Advanced Supersonic Parachute Inflation Research Experiments Pre-flight Trajectory Modeling and Post-flight Reconstruction

Soumyo Dutta*
NASA Langley Research Center, Hampton, VA 23681, USA

Christopher D. Karlgaard† and Jake A. Tynis‡
Analytical Mechanics Associates, Inc., Hampton, VA 23681, USA

Clara O'Farrell§ and Bryan S. Sonneveldt,¶
Jet Propulsion Laboratory, California Institute of Technology, Pasadena, CA 91109, USA

Eric M. Queen‖ and Angela L. Bowes**
NASA Langley Research Center, Hampton, VA 23681, USA

Emily A. Leylek††, and Mark C. Ivanov‡‡
Jet Propulsion Laboratory, California Institute of Technology, Pasadena, CA 91109, USA

The Advanced Supersonic Parachute Inflation Research and Experiments (ASPIRE) was a series of sounding rocket flights aimed at understanding the dynamics of supersonic parachutes that are used for Mars robotic applications. The 2012 Mars Science Laboratory (MSL) had a successful deployment of a supersonic parachute, but based on post-flight analysis of parachute margins, the ASPIRE project was created as a risk-reduction program to improve quantification of these margins and qualify a supersonic parachute for Mars 2020, the follow-on mission to MSL. The first sounding rocket (SR01) flight of ASPIRE occurred near Wallops Island, Virginia on Oct. 4, 2017 and demonstrated the successful deployment and inflation of a MSL build-to-print parachute in flight conditions similar to the 2012 MSL mission. The ASPIRE SR02 and SR03 were successful follow-on flights on Mar. 31, 2018 and Sep. 7, 2018 that demonstrated the new, strengthened supersonic parachute designed for the Mars 2020 project. The SR02 and SR03 parachutes were targeted to 100% and 140% of the expected flight limit load for Mars 2020 to confirm new margins expected from the strengthened parachute. Prior to all flights, a multi-body flight dynamics simulation was developed to predict the

*Aerospace Engineer, Atmospheric Flight and Entry Systems Branch, 1 N. Dryden St., MS 489, AIAA Senior Member.
†Supervising Engineer, AIAA Associate Fellow.
‡Aerospace Engineer, AIAA Member. Employed by Analytical Mechanics Associates, Inc. at the time of the mission.
§Guidance and Control Engineer, Entry, Descent, and Landing Guidance & Control Systems, 4800 Oak Grove Dr. M/S 321-220, AIAA Member.
¶Systems Engineer, Entry, Descent, and Landing Systems & Advanced Technologies, 4800 Oak Grove Dr. M/S 321-220, AIAA Member.
‖Modeling Lead, Aerospace Engineer, Atmospheric Flight and Entry Systems Branch, 1 N. Dryden St., MS 489, AIAA Senior Member.
**Aerospace Engineer, Atmospheric Flight and Entry Systems Branch, 1 N. Dryden St., MS 489, AIAA Member.
††Guidance and Controls Engineer, Entry, Descent, and Landing Guidance & Control Systems, 4800 Oak Grove Dr. M/S 321-220.
‡‡Flight Mechanics Lead, Senior Guidance and Controls Engineer, EDL Guidance & Control Systems, 4800 Oak Grove Dr., M/S 321-220.

parachute dynamics and was used, in conjunction with other tools, to target Mars-relevant flight conditions. After each flight, the on-board data were used to reconstruct the flight trajectory and to validate the pre-flight dynamics simulation. Post-flight analysis showed that all three tests achieved their targeted conditions and pre-flight modeling bounded the key performance metrics for the parachute. This paper describes the flight mechanics simulation, post-flight reconstruction, and the reconciliation process used to validate the flight models.

I. Introduction

In 2017 and 2018, a series of sounding rocket tests to study the dynamics of supersonic parachutes took place at NASA Wallops Flight Facility (WFF). The tests demonstrated successful deployment, inflation, and deceleration by three supersonic parachutes at Mars relevant conditions. The sounding rocket tests were part of the Advanced Supersonic Parachute Inflation Research and Experiments (ASPIRE) program that was started in 2016 to understand the inflation and peak load performance of supersonic parachutes used for NASA Mars robotic missions.

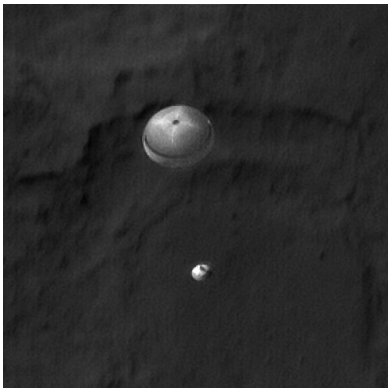

Fig. 1 Mars Science Laboratory DGB parachute and descent stage. (Image Credit: NASA/JPL-Caltech/University of Arizona)

In 2012, the Mars Science Laboratory (MSL) mission had a successful inflation of a supersonic, disk gap band (DGB) parachute which performed nominally on Mars (see Fig. 1) [1]. The Low-Density Supersonic Decelerator (LDSD) program had conducted two flight tests off the coast of Hawaii in 2014 and 2015 with supersonic disksail and ringsail parachutes for Mars applications [2]. Both flight tests suffered parachute failure during the inflation process and raised questions about the understanding of parachute inflation and dynamics at Mars relevant conditions. However, there were critical differences between the MSL parachute and LDSD parachutes. The MSL parachute was a Viking-styled DGB parachute, which differed from the ringsail types used for LDSD, and the MSL parachute was inflated at Mach 1.7 and was 21.35 m in diameter, as opposed to the 30 m diameter parachutes which were inflated at above Mach 2.0 for LDSD.

In 2016, Mars 2020, the follow-on mission from MSL, created the ASPIRE program as a risk reduction exercise. Based on post-flight analysis, it was discovered that the MSL parachute had lower strength margin compared to past Mars missions. In order to gain more margin, a strengthened parachute design was proposed [3]. The goal of the ASPIRE program was to certify a 21.35 m DGB parachute for use at Mars. The ASPIRE project tested two designs: the build-to-print MSL design and strengthened parachute design that increased margins in the strength of the parachute system [3]. The ASPIRE project ultimately had three test flights, with the build-to-print MSL design tested on the first

flight and the new strengthened design tested on the last two flights. The success of the new parachute design led to Mars 2020 adopting the strengthened parachute as its baseline.

To aid in the design of the test trajectories, multi-body dynamics simulations and flight reconstruction tools were created to predict the flight conditions, reconstruct flight conditions from on-board data, and then reconcile flight models to improve the design for the next flight. This paper will provide an introduction to the ASPIRE flight project, its concept of operations, and discuss the flight mechanics models that were used for pre-flight predictions, targeting, and operations. Additionally, the paper will describe the on-board sensors and the reconstruction tool. Finally, the simulation results will be compared with the post-flight reconstructed performance for all three ASPIRE flights.

II. ASPIRE Flight Project

The ASPIRE flight concept of operations is shown in Fig 2. The test vehicle and parachutes were launched on-board NASA Sounding Rocket Operations Contract (NSROC) sounding rockets. For ASPIRE, the sounding rocket stack (as shown in Fig. 3) consisted of a Terrier first stage, a Black Brant IX second stage, and an approximately 1200 kg test vehicle that included the parachute system. The sounding rocket stack was launched and initially spin stabilized. The first and second stage burnout occurred at approximately 5 and 35 s respectively after launch and the payload section separated from the second stage at 104 s. At payload separation, the vehicle nominally was approximately traveling at Mach 1.2 and at 50 km altitude. The test vehicle nominally reached apogee around 51 km, after which the vehicle accelerated as it descended. For ASPIRE SR01, the on-board flight software was programmed to target a dynamic pressure close to MSL-like conditions at full inflation (474 Pa) while being at Mach 1.7 [1]. For SR02 and SR03, the target dynamic pressure was approximately 50% and 100% higher than MSL flight conditions; thus, the target full inflation dynamic pressure was 678 Pa and 949 Pa respectively while the target Mach number at full inflation was still Mach 1.7. After the parachute inflated, the vehicle decelerated rapidly to subsonic conditions and finally splashed down in the Atlantic Ocean approximately 60 km East from WFF. Shortly before splashdown, the vehicle ejected the ballasted nosecone to improve the buoyancy of the rest of the payload. Ballast was added to the nosecone to achieve targets at parachute deployment.

The test vehicle is shown in Fig. 3. The payload is 6.66 m in length and 0.72 m in diameter at its largest cross-section. The front portion of the vehicle consists of the ballast and buoyancy foam, while the back end consists of mortar and other parachute deployment systems. The Gimbaled LN-200 Miniature Flight Computer (GLN-MAC) that is used for triggering events, such as mortar fire, and the NSROC Inertial Attitude Control System (NIACS) were housed in the middle section. The test vehicle is spin stabilized during launch leading up to payload separation and actively controlled by the NIACS from separation to mortar fire using a cold-gas thruster system. In early analysis, it was discovered that active attitude control is needed to maintain the vehicle at the desired attitude for parachute deployment. The NIACS is turned off at mortar fire to allow the dynamics of the parachute and its effect on the test vehicle to be observed without

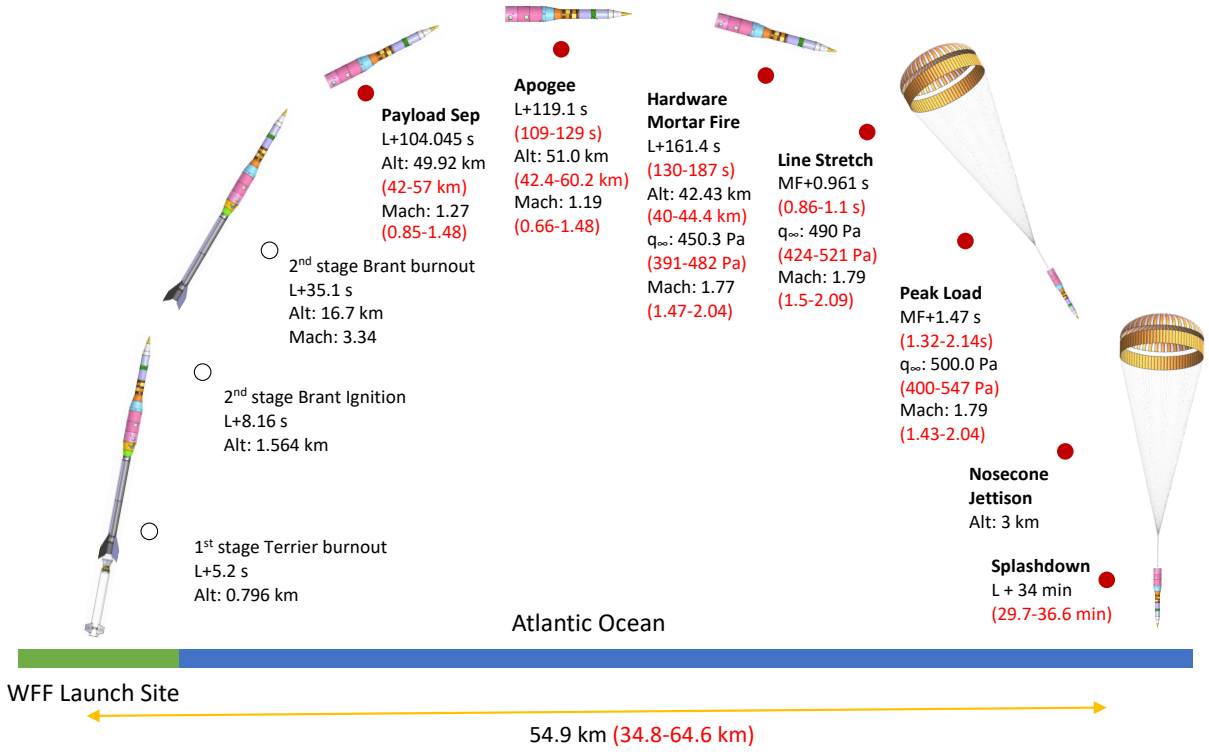

Fig. 2 ASPIRE concept of operations with events modeled in the pre-flight simulation marked with red circle. Reconstructed values in black and pre-flight min/max predictions in red are for SR01 flight. SR02 and SR03 flight conditions are listed in the results section of the paper.

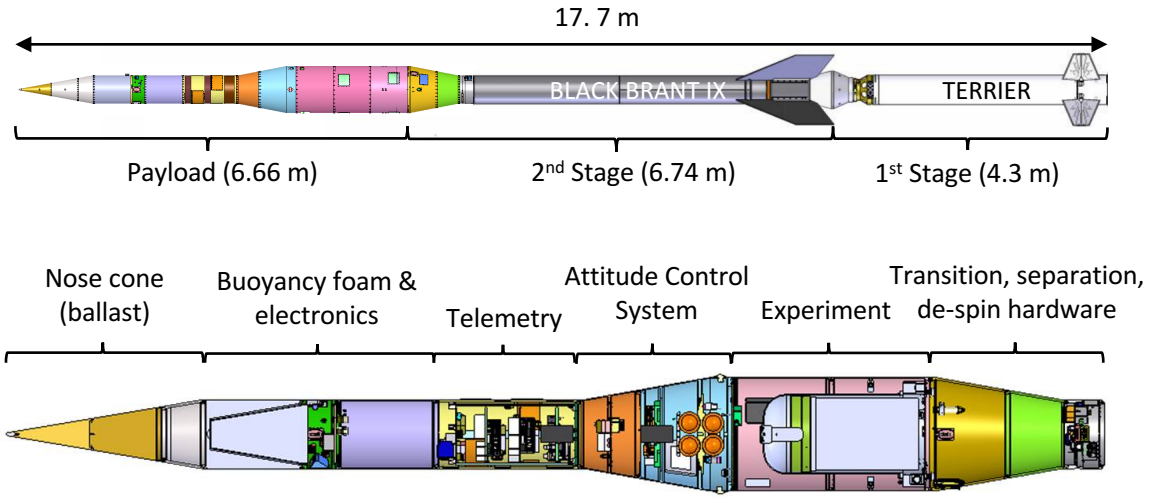

Fig. 3 ASPIRE flight vehicle configuration for SR01.

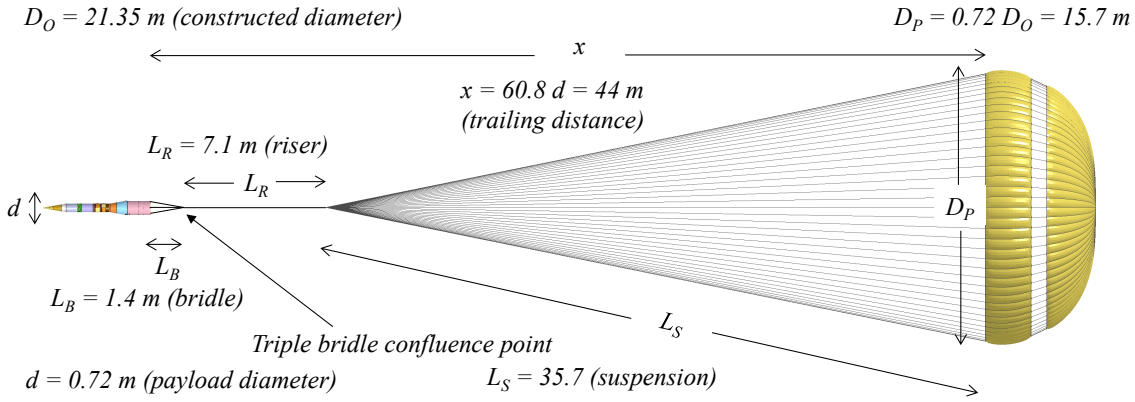

Fig. 4 ASPIRE test vehicle and SR01 parachute system. The dimensions of the SR02 and SR03 parachutes were similar although the fabric and skeletal structure strengths were higher.

any external moments.

The dimensions of the various components of the final test configuration for ASPIRE SR01 are shown in Fig. 4. The constructed nominal diameter of the Viking-scaled parachute for ASPIRE SR01 was 21.35 m and the projected diameter was 15.7 m. For SR02 and SR03, the test article was a strengthened DGB parachute designed for the Mars 2020 mission [3]. The geometric dimensions of the parachute were the same as the SR01 article, although the mass of the parachute was higher due to the use of strengthened materials. Reference [3] discusses the difference between the SR01 and SR02/03 parachutes. For all ASPIRE flights, the test vehicle is attached to the parachute canopy through various lines as shown in Fig. 4. The canopy suspension lines are attached to the triple bridle confluence point (TBCP) via a single riser. Section IV.A discusses the multi-body system modeled in the flight mechanics simulations.

III. Instrumentation and Measurements

A variety of measurement sources were available for use in the trajectory and atmosphere reconstruction process. These measurements included on-board instrumentation such as an Inertial Measurement Unit (IMU) and a Global Positioning System (GPS) receiver; ground-based measurements from tracking radars; and atmospheric soundings from balloons. The reconstruction objectives were to recreate the trajectory and atmosphere experienced by the flight vehicle, so that post-flight analysis could determine if targeted parachute deployment and load conditions were reached. Trajectory reconstruction was conducted primarily with IMU and GPS data, although radar data augmented the trajectory estimate in certain phases of flight. The atmosphere reconstruction was a combination of the sounding data along with post-flight analysis of atmospheric models. The reconstruction methods are discussed in Sec. V, but the following sections provide a more detailed overview of the measurement sources and their performance on the day-of-launch.

A. Inertial Measurement Unit

Three-axis linear accelerations and angular rates were measured by the GLN-MAC inertial navigation system, which contains three-axis solid-state silicon Micro Electro-Mechanical System (MEMS) accelerometers and three-axis solid state fiber-optic gyroscopes. The GLN-MAC uses an electric motor to counter-rotate the internal mount plate such that the LN-200 senses a low rotational rate about the spin axis. The gimbaling has the effect of reducing error buildup due to scale factor uncertainties in the roll gyro.

The GLN-MAC produces two sets of telemetry, one from the gimbaled LN-200 at a rate of 400 Hz and one from the integrated GLN-MAC system at a rate of 100 Hz. The resolver angle, which is the roll angle of the gimbal, is also telemetered at a rate of 400 Hz. The GLN-MAC level outputs utilize the resolver angle and resolver rate to generate an equivalent strapdown representation of the gimbaled LN-200 accelerations and rates. IMU data for strapdown systems, where the IMU is attached directly to the vehicle and does not have a differential movement relative to the vehicle, can be directly integrated to provide trajectory; hence, this adaption for GLN-MAC transforms rotating IMU data into an easier representation. Typical performance characteristics of the GLN-MAC sensor can be found in [4].

There were intermittent dropped packets of data from the GLN-MAC telemetry, but these were isolated to single time points and thus did not degrade the reconstruction for SR01 and SR03. There were several time points, of the order of a few tenths of seconds, where there were dropouts in the data toward the end of the trajectory in the SR02 data. The reconstruction method (see Sec. V for more information) relies on monotonic integration of the IMU data to calculate the trajectory, and having data dropouts means the algorithm has time gaps in the integration. The dropouts meant there was uncertainty in what actually occurred during the gaps in the data, so to reflect that increased uncertainty, the SR02 data required manual tuning of the process noise covariance used in the post-flight reconstruction Kalman filter. The tuning accounted for the increased uncertainties in the numerical integration of the equations of motion during the prediction step due to missing data. No such tuning was required for the SR01 and SR03 flights. The cause of the dropouts was not identified although such dropouts can be common on sounding rocket flights. Both the telemetered and on-board data had the dropouts.

B. Global Positioning System

Measurements of position and velocity were obtained from a Javad TR-G2 HDA GPS receiver at a rate of 20 Hz. A wraparound GPS antenna was used on the vehicle, which enabled continuous GPS coverage during the high spin rate of the powered flight phase. The Javad unit also produced estimates of the uncertainties in the position and velocity solution based on the number of satellites in view and the corresponding geometry. Performance of the Javad unit was similar across all three flight tests, tracking between 9-12 satellites and producing solutions with position and velocity 1σ uncertainties on the order of 1.5 m and 0.5 cm/s, respectively [5, 6].

C. Tracking Radar

Tracking of the sounding rocket and payload was provided via a C-band transponder and skin track of the vehicle from three primary radars, WFF Radars 3, 5, and 18. The radar data consisted of slant range, range rate, and azimuth and declination from the radar station to the vehicle. The data was provided at 50 Hz for all flights. For SR03, an additional track from WFF Radar 2 was provided which was not available during the earlier flights. The geometry of the radar stations relative to the as-flown SR03 trajectory is shown in Figure 5.

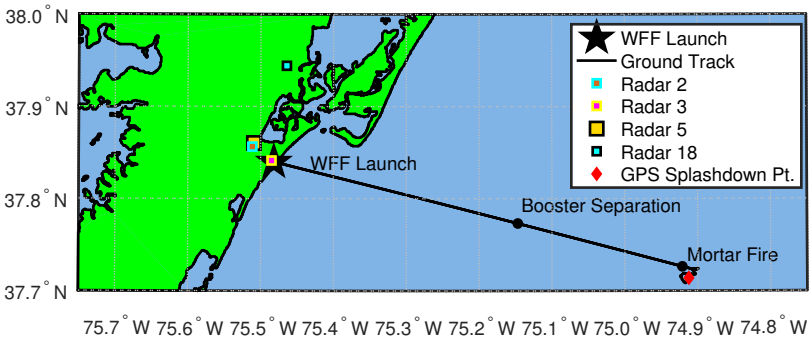

Fig. 5 ASPIRE SR03 ground trace and radar geometry. The tracking geometry was similar for SR01 and SR02 with the exception of Radar 2.

As discussed later in Sec. V, trajectory reconstruction is done primarily with IMU and GPS data, but where radar data is available, uncertainty in the reconstruction could be improved. For sounding rocket flights, often radar data show dropouts and the tracking data require some editing. Since radar data are an auxiliary not primary data source for trajectory reconstruction, the dropouts have minimal effect on the uncertainty of the estimated trajectory. During SR01, all three radars that tracked the vehicle exhibited several dropouts or loss of transponder lock over the trajectory that made the data unusable. Data from some portions of the flight were manually edited out and not utilized for reconstruction. The SR02 flight test had similar radar performance with one radar maintaining lock during the entire trajectory while the two other radars having dropouts that led to manual editing of their data before reconstruction. Fortunately, in the case of SR03, all four radars maintained lock on the tracking beacon for the duration of the flight. For each flight test, all data with elevation angles of less than 1° were removed from the reconstruction process because of increased noise due to refraction errors.

D. Meteorological Data

Knowledge of the atmospheric state at the time of testing was required in order to determine the conditions at parachute deployment (Mach number and dynamic pressure), examine the aerodynamic performance of the payload and parachute, as well as evaluate the performance of the triggering scheme. Specifically, vertical profiles of the atmospheric temperature, pressure, density, and winds spanning from the surface to an altitude of approximately 55 km were required.

These profiles were derived using a combination of measurements from radiosondes deployed on meteorological balloons and a meteorological analysis from the Goddard Earth Observing System Model, Version 5 (GEOS-5).

Meteorological balloons were released at regular intervals prior to the sounding rocket launch, and reached altitudes of 35-40 km. Four balloons were used for SR01, five for SR02, and six for SR03. The 3 kg latex balloons were filled with sufficient helium to provide 1.8 kg of free lift and released from ground altitude. Each balloon carried a single Lockheed Martin Sippican (Marion, MA) LMS-6 radiosonde. Because the balloons were not expected to reach altitudes above 40 km, the GEOS-5 profiles on the day-of-launch were used to augment the atmospheric profiles above 40 km.

E. Other Instrumentation

The vehicle also contained other science instruments, such as three situational cameras, three high-speed, high-resolution science cameras, and load cells used to measure the parachute tension forces. These instruments were not used directly in the trajectory reconstruction effort described in this paper. Reference [7] provides details about these science instrumentations.

IV. Pre-flight Trajectory Simulation Detail

Flight mechanics simulations that modeled the flight profile from launch to splashdown provided vehicle performance predictions and information to target the mortar fire trigger for desired parachute performance. The powered portion of the flight profile was handled by WFF tools, while the test portion of the flight, from ASPIRE separation to splashdown, were modeled by two other flight mechanics simulations. These two flight mechanics simulations – Program to Optimize Simulated Trajectories II (POST2) and Dynamics Simulator for Entry, Descent, and Surface Landing (DSENDS) – were used in concurrence to develop flight parameters and inform stakeholders, while providing verification to each other during the development. There are subtle differences between the two simulations; in this paper the focus is on the POST2-based simulation that provided multi-body predictions for the ASPIRE flights. The reader is referred to Refs. [8, 9] for information about the DSENDS simulations for similar flight mechanics problems.

The POST2 program is a six degree-of-freedom (6-DOF) flight dynamics simulation tool that can simultaneously simulate the trajectory of up to 20 independent or connected rigid bodies. It is a generalized point mass, discrete-parameter targeting and optimization trajectory simulation program with multi-vehicle capabilities that integrates translational and rotational equations of motion along the trajectory. The simulation tool has significant entry, descent, and landing (EDL) flight heritage as it has been used in the past successfully for several Mars EDL missions, such as Mars Pathfinder [10], Mars Exploration Rovers [11], Phoenix Mars Scout [12], and Mars Science Laboratory [13]. Additionally, POST2 simulations were used on LDSD flights 1 [14–16] and 2 [17, 18].

The ASPIRE POST2 simulation was based on the tools used for LDSD. The simulation incorporated various engineering models for vehicle mass properties, mortar fire orientations, computational fluid dynamics (CFD)-based

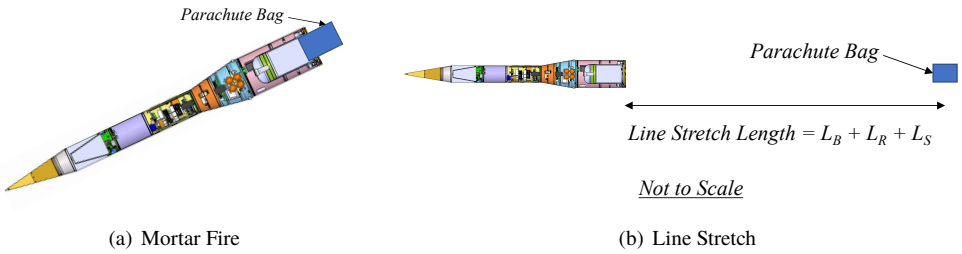

(a) Mortar Fire (b) Line Stretch

Fig. 6 Multi-body model dynamics for ASPIRE.

aerodynamic predictions of the test vehicle, parachute aerodynamics based on wind tunnel tests, flight software used for triggering during flight, ACS thruster controller algorithm, and atmospheric property predictions from Earth Global Reference Atmospheric Model (Earth-GRAM 2010) [19] and NASA Goddard Earth Observing System model version 5 (GEOS-5) [20]. The models and their uncertainties were varied in a Monte Carlo fashion to provide statistical estimates of various flight performance parameters, such as trajectory conditions at parachute full inflation and splashdown predictions.

A. Multi-Body Dynamics

The POST2 multi-body dynamics model is based on simulating the response between two rigid, 6-DOF vehicles connected by lines. For ASPIRE, the two 6-DOF rigid bodies are the test vehicle and the parachute, which are connected by tension-only bridle lines that have stiffness and damping. Treating the parachute as a rigid vehicle is a key assumption because it is modeled as a single vehicle from the TBCP up to the canopy with mass properties that include the mass of the canopy, suspension lines, and riser lines. In reality, the parachute is a flexible body and the suspension lines and riser line also have their own mass, stiffness, and damping. However, multi-body simulations used for other flight projects in the past have shown that modeling the parachute down to the TBCP as a rigid body and then connecting that body to the forebody via tension-only bridle lines provides attitude and force response that is comparable to flight data [1]. Thus, for ASPIRE, the same assumptions were made.

The multi-body phase of the modeling starts at mortar fire, when a test vehicle ejects the parachute bag using the mortar. The mortar is modeled as a thruster that applies a constant force on both the parachute bag vehicle and the test vehicle for a finite time. The mortar thrust direction can be varied based on alignment uncertainty for Monte Carlo analysis. The parachute bag, which is a three degree of freedom (3-DOF) vehicle, is pushed along the length of the parachute can until it fully exits from the separation plane of the test vehicle. While the bag is in the parachute can, a constraint force equations (CFE) based model [21] is used to constrain the motion of the bag axially and also simulate the friction on the bag. The initial phase of the multi-body dynamics is shown in Fig. 6(a).

After the parachute bag exits the test vehicle, the only force acting on the bag is gravity. Although in reality the bag experiences aerodynamic drag, this force model is very difficult to model with CFD tools especially since the bag is in

the unsteady wake of the test vehicle. Assuming the bag experiences no drag means the bag continues at similar relative velocity as the test vehicle instead of slowing down and growing the relative distance if drag was modeled. Thus, the separation distance between the bag and the payload vehicle grows slowly with the no drag assumption, providing a larger estimate of the time to the line stretch event. Pre-flight testing had shown very little sensitivity to the performance results due to this assumption and reconstruction results from the flights (shown in Sec. VI) show that the prediction line stretch times in the simulation matched observed data.

Upon reaching the line stretch distance, shown in Fig. 6(b), the parachute bag vehicle is replaced by the 6-DOF rigid parachute body. The line stretch distance is the sum of bridle lines length (L_B), riser line length (L_R), and suspension lines length (L_S). Recall, the parachute vehicle starts at the TBCP, where the three bridle lines provide the connection to the test vehicle via tension-only lines. The stiffness and damping of the tension lines are based on line properties of the actual bridle lines. The attitude of the parachute vehicle is initialized at a prescribed angle relative to the payload that is varied in a Monte Carlo simulation. This angle is empirically informed by previous flight data and wind tunnel tests. However, most DGB test data consist of a blunt body forebody similar to entry aeroshells. Blunt bodies have larger wakes than the relatively slender body of the ASPIRE test vehicle. Thus, the parachute initialization angle choice for ASPIRE was a informed by previous data and engineering judgment. The flight data and ensuing reconstruction from each flight informed the initial parachute angle for the next ASPIRE flight.

Once the line stretch conditions are achieved and the parachute vehicle has been initialized, the two rigid bodies behave under their separate aerodynamics albeit responding to each other due to forces from the lines connecting them to the TBCP. The test vehicle aerodynamics and ASPIRE parachute aerodynamics are discussed by Muppidi et. al. [22, 23] and O'Farrell et. al. [24, 25] However, some mention of the parachute aerodynamics is necessary to describe the multi-body model. The parachute aerodynamics consists of 6-DOF aerodynamic coefficients, such as tangential force, normal force, and pitching moment coefficient. The vehicle is treated as an axisymmetric body. The aerodynamics are a function of Mach number and angle of attack. During inflation, the parachute aerodynamic force changes from zero at line stretch to peak load at full inflation. The force is based on a power law dependent on time since line stretch and time to full inflation [26]. The inflation time itself is based on the distance it takes for the parachute to travel a fixed inflation distance [27], which is determined empirically and varied in Monte Carlo analysis.

After the full inflation time has elapsed, the configuration in the simulation looks similar to what is shown in Fig. 4. At full inflation, other models are turned on in the simulation. The parachute has inflated by capturing a volume of atmosphere. This captured atmosphere adds to the parachute mass as so-called apparent mass. These forces are activated at full inflation since their effects are captured during the inflation process by the value of opening load factor that is applied to the aerodynamic force. Additionally, while the parachute vehicle is above Mach 1.4, it experiences areal oscillation. Cruz et. al. discuss the parachute model in great detail in Ref. [26], while Way describes the inflation dynamics in Ref. [28]. These models were evaluated post-flight with reconstructed trajectory information.

B. Flight Software and NIACS Modeling

Active attitude control was necessary between payload separation and mortar fire to maintain desired attitude at parachute deploy. In the vehicle, attitude control was maintained using the NIACS. A high fidelity model of the NIACS firings was implemented in the simulation to capture how the test vehicle attitude would be maintained and to provide vehicle flight engineers an avenue to test NIACS control gains. The flight software provided the NIACS commands when the simulation provided inputs with the vehicle position, velocity, attitude, and attitude rate history at 100 Hz. This section describes the various components of the NIACS model and how they were integrated into the pre-flight simulation.

The GLN-MAC was a primary component of the NIACS, which was located on the attitude control system (ACS) section of the payload (Fig. 3). The NIACS consists of the GLN-MAC and a set of cold-gas thrusters. A set of four cold-gas thrusters located at 90° intervals around the circumference of the experiment section were used to maintain a near-zero total angle of attack, pitch rate, and yaw rate leading up to parachute deploy. Two pairs of roll-axis thrusters (a clockwise pair and a counter-clockwise pair) were used to null any residual roll rate following de-spin and separation from the second stage.

The NIACS cold-gas actuators that are modeled in the simulation are fired based on the commanded values from the flight software. The NIACS actuators consist of four roll thrusters (two for clockwise and two for counter-clockwise control), four thrusters for pitch and yaw control at a low level, and four additional thrusters for pitch and yaw control at a higher (or super) level. A delay between the NIACS command and the actuator action is modeled to match previously observed delay in NIACS flight data. Moreover, when multiple thrusters are firing, there is a decrement in thrust due to total pressure drop in the lines, which is also captured in the actuator model.

The NIACS was also responsible for triggering the firing of the parachute mortar at the desired dynamic pressure. During flight, the NIACS computed an on-board vehicle state from the IMU measurements and GPS-derived position and velocity. This navigation solution provided an estimate of the inertial velocity and altitude throughout the flight. Prior to launch, polynomial models for atmospheric winds, density, and temperature as a function of altitude were loaded onto the NIACS. These polynomials were then evaluated during flight using inertial states to obtain an on-board estimate of the wind-relative dynamic pressures which was used to trigger parachute deployment. Simulations of the payload trajectory along with estimates of the time from mortar fire to peak load were used to derive the NIACS trigger value. Once that dynamic pressure was calculated, the NIACS initiated a series of events, including turning off the ACS, starting the high speed camera recording, deploying the camera lens covers, and mechanical trigger delay after the dynamic pressure trigger was reached, signaling of the mortar to fire.

Models such as the NIACS and the multi-body dynamics allow the flight mechanics simulation to create predictions for various phases of flight. Of special interest are states at mortar fire, where the parachute deployment event is triggered, and full inflation, where Mars-relevant conditions are to be met as part of experimental objectives for ASPIRE.

In subsequent sections, these pre-flight predictions are compared with the reconstructed values from the ASPIRE flights.

C. Operations Support

A key requirement of the ASPIRE simulations was to provide day-of-launch and operations support. The day-of-launch support was conducted by gathering forecast atmospheric profiles, creating polynomials that represented these forecast atmospheric profiles for the flight software, and then using these polynomials in simulation to target dynamic pressure. During analysis done before SR01, it was found that the daily shift in atmospheric properties, such as winds, affected the splashdown prediction of the test vehicle appreciably and changed the target conditions needed to hit the MSL-like flight conditions. Thus, a system was created where the forecast GEOS-5 atmosphere [20] for the day-of-launch and time-of-launch would be downloaded at multiple times one day before launch (L-1 predictions). Using the L-1 prediction 24 hours before the flight for the targeted flight time (8:00 AM at WFF), the flight constants such as the atmospheric polynomials and the target conditions were generated and passed on to the flight operations team. The flight performance was monitored with updated inputs to the flight simulations that used more recent atmospheric predictions to understand if the changing atmospheric conditions were moving the flight vehicle outside the bounds of requirements. Then on the day of launch, estimated splashdown latitude, longitude, and time were provided with the latest atmospheric predictions; these splashdown predictions were passed on to the vehicle recovery team while the vehicle was on the parachute. A recovery zone estimate was also made using forecast atmosphere from two days before the launch (L-2) to meet range safety requirements, such as that splashdown occurs within the range that had been evacuated for safety.

The baseline plan through the first two flights was to target a launch using 8:00 AM local time forecasts; however, SR02 flew at 12:19 pm due to concerns regarding the sea states. The flight targets were tuned for a different launch time and there was a noticeable effect on the flight performance. This discrepancy is discussed in Section VI.B. Thus, the targeted states and polynomials for SR03 were created for two target times – 8:00 AM and 11:00 AM local time. Various flight simulation runs were scheduled daily to test the 8:00 AM targets for a later launch time. Then, the day before launch, polynomials were selected for the target time closest to the expected launch time.

V. Reconstruction Methods

The instrumentation utilized during the ASPIRE missions provided an extensive set of measurement data from which reconstruction was performed. Accurate reconstruction is important in order to gauge if the targeted conditions of the flight were achieved and to use the flight data to develop models of parachute performance. It is important to have data, methods, and models with low uncertainty to ensure the reconstructed flight data is reliable. The following section describes the methodologies used to reconstruct the trajectory and atmosphere given the measurements taken during flight.

A. Atmosphere Reconstruction

1. Weather Balloon Measurements

Temperature, humidity, and altitude were measured on the weather balloons using on-board instrumentation, and the atmospheric winds were derived from the GPS velocity measurements. The atmospheric pressure was derived from the temperature and altitude measurements by assuming that the atmosphere was in hydrostatic equilibrium, a typical assumption made for flight applications.

Table 1 lists the uncertainties associated with the radiosonde measurements, at the $3-\sigma$ level. Where the uncertainties were not stated by the manufacturer [29], the values for radiosondes of the same class from the 2014 World Meteorological Organization (WMO) report on atmospheric measurement techniques [30] were used as an example. Figure 7 shows the temperature and east wind measurements recorded at 3, 2:25, 1:45, and 1 hours before the SR01 launch as an example. The wind measurements have been low-pass filtered with a cut-off frequency of 1/600 Hz, to yield a wavelength of approximately 1 km in the vertical direction.

Table 1 LMS-6 measurement 3-σ uncertainties

Measurement	Uncertainty	Notes
Temperature	0.45 K	[29]
Humidity	7.5% RH	Valid to P = 20 hPa [29]
Wind Velocity	1.65 m/s	Vector magnitude [30]
Pressure ($P > 100$ hPa)	1.8 hPa	[30]
Pressure (10 hPa $< P <$ 100 hPa)	0.6 hPa	[30]
Pressure ($P < 10$ hPa)	0.075 hPa	[30]

2. Atmospheric Model

Since the meteorological balloons have a burst altitude of approximately 40 km, no in-situ measurements were available above this altitude. Therefore, the atmospheric profile above 40 km was obtained from a GEOS-5 analysis. The GEOS-5 analysis is a retrospective assessment of the prediction and includes data from meteorological observations to describe the best estimate of the actual atmospheric quantities [31].

The GEOS-5 analysis of the atmospheric state is calculated daily at three hour intervals, starting at 0:00 UTC. The analyses are produced on a grid with a horizontal resolution of 0.5° in latitude and 0.625° in longitude. Vertical profiles are output at 42 pressure levels ranging from 1000 hPa near the surface to 0.1 hPa (approximately 65 km above sea level) [32]. For SR01, the GEOS-5 analysis for 12:00 UTC (8 am local time at WFF) was used to obtain vertical profiles for the atmospheric temperature, pressure, density, and winds at the grid location closest to Wallops Island: (37.75° N, 75.0° W). Similarly, SR02 used the GEOS-5 analysis for 15:00 UTC (11 am local time at WFF) and SR03 used

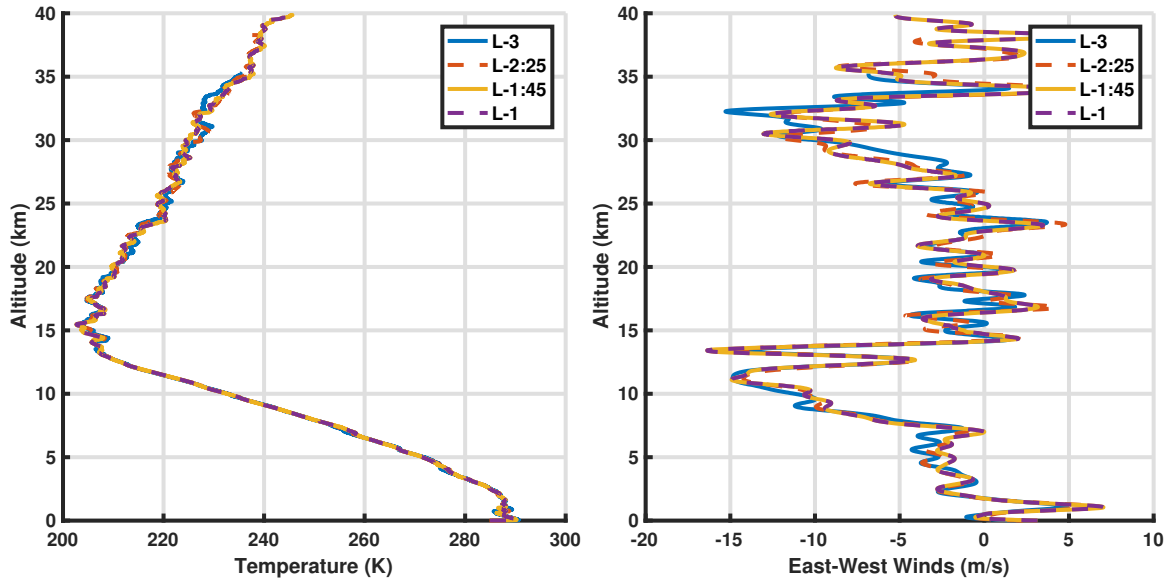

Fig. 7 SR01 radiosonde measurements.

the GEOS-5 analysis for 12:00 UTC. For each test flight, a balloon measurement profile was used for the as-flown atmosphere model up to its maximum altitude. The GEOS-5 analysis model was used for altitudes above this threshold.

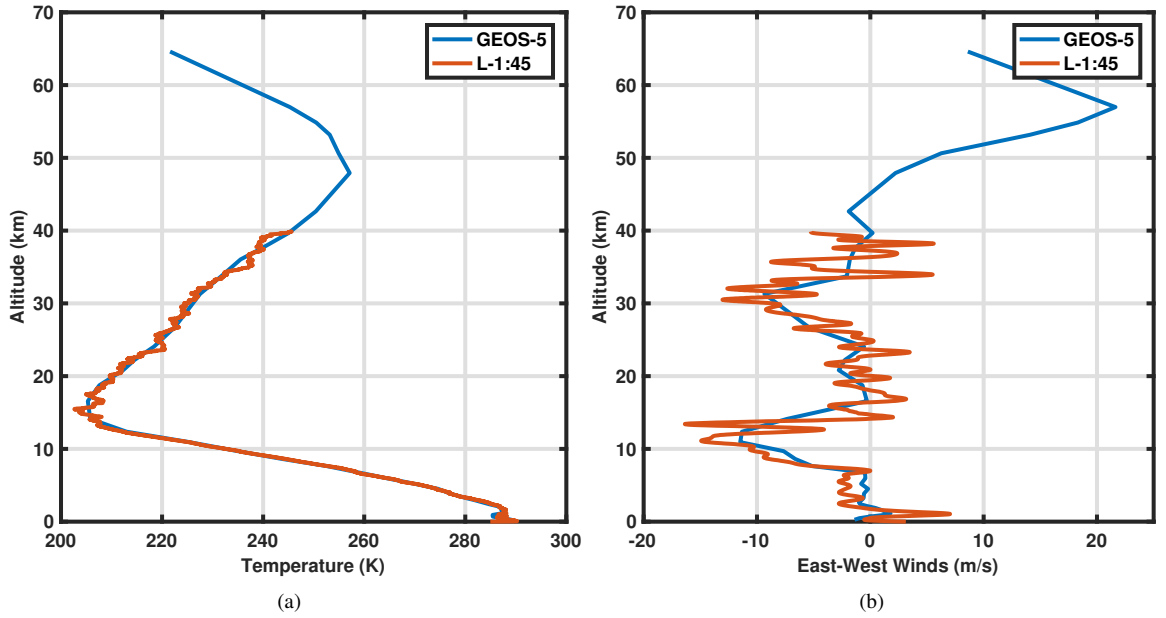

Fig. 8 GEOS-5 analysis for 12:00 UTC on the day-of-launch of SR01. The measurements from the L-1:45 radiosondes, which reached the highest altitude, are shown in blue for comparison.

Figure 8 shows the vertical profiles of temperature and east wind for the 12:00 UTC GEOS-5 analysis for SR01. Below 39.9 km, the GEOS-5 results are compared against the measurements from the L-1:45 radiosonde, which reached

the highest altitude. In general, the GEOS-5 profile captures the mean of the radiosonde measurements. However, the radiosonde measurements exhibit small-scale variations that are not captured by GEOS-5. The variations in the winds can be large, leading to differences between the GEOS-5 profile and measurements in excess of 10 m/s. The differences between the radiosonde temperature measurements and the GEOS-5 profile are significantly smaller (less than 4 K), and the GEOS-5 temperature profile does not show a bias relative to the measurements. The radiosonde pressure and density measurements are also in close agreement with the GEOS-5 profile, because the radiosonde pressure and density measurements are integral functions of temperature and the measured temperature follows the GEOS-5 profiles. The impact of the radiosonde and GEOS-5 differences are small for the trajectory, since the most scientifically significant portions of the flight occur above 40 km altitude.

B. Trajectory Reconstruction

The ASPIRE trajectory reconstruction was performed using a Matlab-based Iterative Extended Kalman Filter (IEKF) code known as New Statistical Trajectory Estimation Program (NewSTEP) [2, 33, 34]. This software is a generalization of the Statistical Trajectory Estimation Program (STEP)[35, 36] that was developed by NASA Langley Research Center and applied to launch and entry vehicle trajectory reconstruction analyses during the 1960s-1980s. The NewSTEP code borrows largely from STEP, but includes various enhancements to the core code that have been developed to accommodate the reconstruction needs of recent flight projects.

The NewSTEP tool was configured to process data from the GLN-MAC gimballed IMU measurements using a process developed for LDSD [2]. Many past applications of gimbaled IMU reconstructions have made use of an equivalent strapdown representation of the linear accelerations and angular rates in the estimation filter by transforming the platform data into a strapdown frame via the measured gimbal angle [37, 38]. This approach has the advantage of producing a strapdown representation of the inertial measurements without any error buildup due to roll gyro scale factor. However, the reliance on using the resolver angle to transform IMU data in a rotating frame to a non-rotating frame means that there is sensitivity to resolver angular rate and acceleration uncertainty. Any measurement error in the resolver angle, such as resolver angle quantization, will be amplified by errors from numerical differentiation when the angle is converted to rates and acceleration that is needed for the rotating frame to non-rotating frame transformation.

An alternate approach was devised in which the trajectory of the LN-200 itself was reconstructed from the measurement data using the Kalman filter approach to blend IMU measurements with GPS and radar. The output of this process is a kinematic reconstructed trajectory of the LN-200 in an IMU-relative frame through inertial space. After reconstructing the LN-200 trajectory, the resolver angle profile was used to transform the state outputs into the vehicle aerodynamic coordinate frame. Additionally, the reconstructed mass properties were incorporated in order to translate the reconstructed state of the vehicle to the center of gravity (cg). The pre-flight mass estimates were used for the reconstruction, but the timeline of the mass properties changing as stages were jettisoned were adjusted to match the

as-flown timeline.

At this point in the process, the resolver quantization uncertainty corrupts the reconstructed vehicle state, but this uncertainty is an algebraic mapping at each instant in time such that the resolver angle uncertainties do not propagate over time. After transforming the LN-200 state to the vehicle body frame at the cg, the freestream atmosphere was computed as a function of altitude from a table lookup, and the atmospheric relative state (angle of attack, Mach number, dynamic pressure, etc.) was computed.

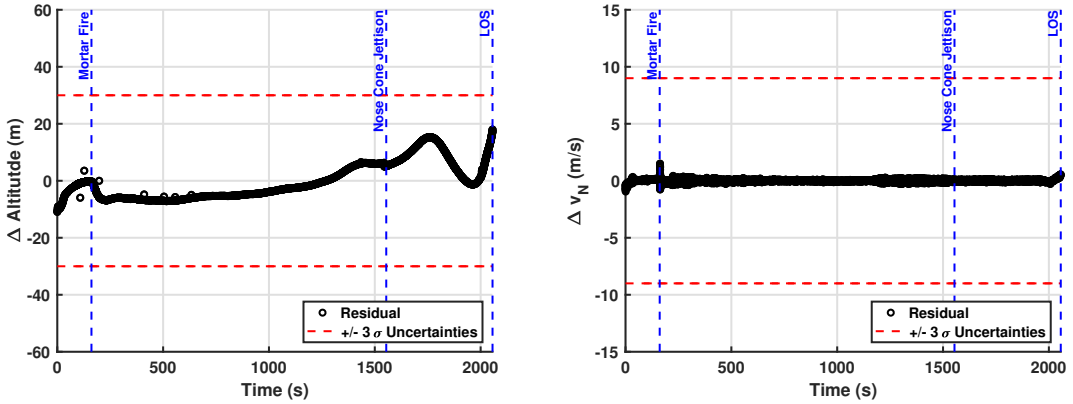

(a) Geodetic Altitude Residuals

(b) North Velocity Residuals

Fig. 9 ASPIRE SR01 GPS measurement IEKF residuals

The GPS residuals are computed by taking the difference between the measurement observed during flight and the predicted measurement generated by the filter. An inspection of the measurement residuals provides an assessment of the filter performance relative to the measurement uncertainties. The GPS measurement residuals for SR01 are shown in Figure 9. It is evident that the residual values largely fall inside of the 3σ uncertainties, which is an indicator of good filter performance. The filter residuals were similar for all three flight tests.

VI. Flight Mechanics Predictions and Reconciliation with Flight Data

In the following sections, ASPIRE best estimated trajectories (BET) are compared with pre-flight Monte Carlo estimates. In most instances, the reconstructed flight conditions fell well within the pre-flight Monte Carlo distributions that provided statistical estimates of conditions at major events of interest. However, in cases where the pre-flight estimates fail to match the reconstruction, the process of reconciliation was undertaken to adjust the pre-flight models to understand what components of the simulation should be modified to improve predictions for subsequent flights. Only a subset of the reconstruction data from the ASPIRE flights are covered in this paper; more reconstruction data are present in Refs. [6, 7, 24, 25, 39–41].

A. ASPIRE SR01 Reconstruction and Reconciliation

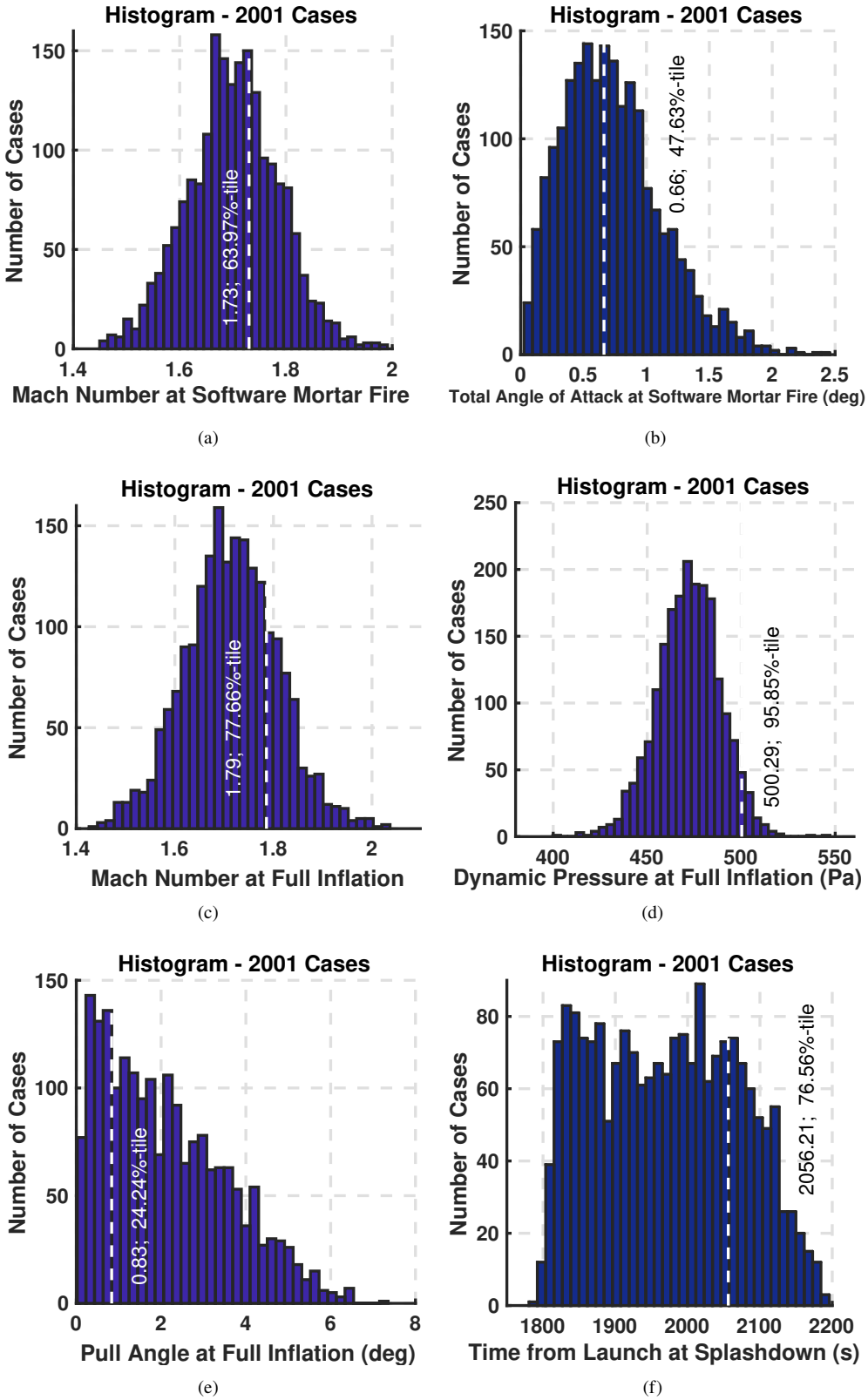

Fig. 10 Pre-flight Monte Carlo predictions (histograms) and comparison to reconstruction (white line) for ASPIRE SR01.

Figure 10 compares histograms of pre-flight parameters to the post-flight BET reconstructed value (vertical white line). The pre-flight predictions are a result of Monte Carlo analysis where various simulation settings, like atmosphere, aerodynamics, mass properties were dispersed randomly for 2000 cases to aggregate statistics about events of interest. The reconstructed BET values are listed as percentiles of the Monte Carlo result, where a low or high percentile denotes that the reconstruction is a low probability event, while a percentile close to 50 denotes that the value is close to the median of the prediction and is thus a high probability event. In general, as one approaches the tails of a Monte Carlo distribution, the probability decreases greatly, and so a small percentile difference in the tails of a distribution corresponds with a large probability difference of that event according to the distribution.

The reconstructed trajectory of the ASPIRE SR01 prior to payload separation is summarized in Table 2. Recall that the flight simulation modeled dynamics post-separation from the sounding rocket. However, based on predictions from WFF, the Brant stage over-performed, leading to higher velocity and energy at its burnout, which in turn led to higher velocity at payload separation and apogee.

Table 2 ASPIRE SR01 trajectory conditions prior to payload separation

Event	**Time from Launch** *sec*	**Mach**	**Dynamic Pressure** *Pa*	**Wind-Relative Velocity** *m/s*	**Geodetic Altitude** *km*	**Flight Path Angle** *deg*
Launch	0.00	0.01	8.07	3.61	-0.02	36.2
Spin Up	1.18	0.21	3070.38	70.52	0.02	79.8
Terrier Burnout	6.23	0.80	41108.93	273.26	1.06	76.3
Brant Ignition	8.02	0.74	33481.89	253.30	1.52	74.7
Mach 1	11.98	1.00	52824.66	338.08	2.64	71.7
Mach 2	23.16	2.00	112192.78	637.46	7.64	67.1
Mach 3	30.04	3.00	126143.61	876.17	12.37	64.9
Brant Burnout	34.27	3.40	89587.04	979.30	15.97	64.1
Despin Begin	100.09	1.32	102.08	423.54	49.27	25.4

Table 3 shows reconstructed trajectory results and its pre-flight predictions for events after ASPIRE separation from the sounding rocket. The table also includes the percentile that the flight reconstruction represents of the pre-flight prediction. The flight mechanics simulation pre-flight predictions mostly agree with the reconstructed BET. The reconstructed Mach number, total angle of attack, parachute pull angle, and splashdown time are all within a high confidence area of the pre-flight prediction. The dynamic pressure at full inflation is at a lower probability (96th percentile) within the pre-flight estimates, but since the Mach number is not a low probability event, it suggests that there is difference between the pre-flight estimate of the atmospheric density and what was seen in flight.

Table 3 ASPIRE SR01 pre-flight prediction and reconstruction of post ASPIRE separation

Item	Units	Pre-Flight Prediction			Flight	Percentile
		1%-tile	50%-tile	99%-tile		
Payload separation						
Mach		0.98	1.18	1.39	1.27	83.36
Dynamic pressure	Pa	31.37	67.68	153.16	87.15	76.86
Wind-relative velocity	m/s	312.49	378.46	446.04	407.80	84.56
Geodetic altitude	km	45.28	50.22	55.47	49.92	44.13
Flight path angle	deg	13.20	23.38	35.49	20.60	27.09
Apogee						
Time from launch	s	113.24	119.85	126.82	119.04	38.43
Mach		0.81	1.07	1.29	1.19	87.56
Dynamic pressure	Pa	14.01	48.38	131.94	65.74	74.46
Wind-relative velocity	m/s	255.03	342.70	416.19	379.66	86.46
Geodetic altitude	km	45.69	51.43	57.96	51.00	43.18
Mortar fire						
Time from launch	s	145.44	163.99	181.32	161.41	36.28
Mach		1.53	1.74	1.95	1.77	64.57
Dynamic pressure	Pa	410.94	438.35	464.58	452.53	88.96
Wind-relative velocity	m/s	482.11	551.33	620.17	560.29	62.62
Geodetic altitude	km	40.45	42.12	43.69	42.40	65.22
Flight path angle	deg	-60.25	-50.29	-37.57	-46.40	78.31
Line stretch						
Time from launch	s	146.40	164.97	182.29	162.37	36.28
Mach		1.56	1.77	1.99	1.79	58.52
Dynamic pressure	Pa	448.50	482.28	513.28	491.82	75.66
Wind-relative velocity	m/s	491.49	560.56	630.86	567.74	59.72
Geodetic altitude	km	40.11	41.71	43.18	42.01	67.17
Flight path angle	deg	-60.70	-50.89	-38.40	-47.10	78.16
Full inflation						
Time from launch	s	147.34	165.70	182.97	162.88	35.13
Mach		1.49	1.71	1.94	1.77	72.26
Dynamic pressure	Pa	430.42	472.50	509.35	494.88	95.85
Wind-relative velocity	m/s	470.78	541.98	618.00	560.94	73.11
Geodetic altitude	km	39.85	41.38	42.88	41.80	74.66
Flight path angle	deg	-61.11	-51.38	-39.22	-47.40	79.76
Parachute load	lbf	30,879	35,666	40,204	32,387	5.05
Mach 1.4						
Time from launch	s	147.72	166.85	185.14	164.34	36.73
Dynamic pressure	Pa	291.76	335.33	398.93	334.20	48.38
Wind-relative velocity	m/s	436.88	441.83	446.77	443.43	78.61
Geodetic altitude	km	39.73	40.93	41.90	41.26	77.26
Flight path angle	deg	-62.43	-52.16	-39.81	-48.90	75.46
Mach 1.0						
Time from launch	s	150.07	169.49	188.15	166.99	36.98
Dynamic pressure	Pa	168.28	190.81	221.73	188.93	43.38
Wind-relative velocity	m/s	310.71	314.72	318.29	315.52	69.97
Geodetic altitude	km	39.09	40.15	41.03	40.49	80.66

Item	Units	Pre-Flight Prediction			Flight	Percentile
		1%-tile	50%-tile	99%-tile		
Flight path angle	deg	-65.47	-54.62	-41.17	-52.90	64.27
Nose cone jettison						
Time from launch	s	1375.57	1487.22	1651.15	1554.09	77.46
Mach		0.03	0.03	0.03	0.03	12.39
Flight path angle	deg	-87.31	-69.37	-47.99	-85.20	3.40
Splashdown						
Time from launch	s	1806.23	1971.04	2170.01	2056.19	76.51
Mach		0.02	0.02	0.02	0.02	99.10
Flight path angle	deg	-86.24	-60.96	-31.59	-41.20	93.60

For reconciliation, two pre-flight Monte Carlo settings were adjusted that were not known *a priori* to compare simulation results with reconstruction. The atmosphere used in the pre-flight simulations were GEOS-5 forecasts. Post-flight, the reconstructed atmosphere [5] was available for use in the Monte Carlo. Additionally, post-flight the exact state of the vehicle at separation (the initial condition of the simulation) was known due to flight navigation states. When these two model settings were adjusted in the simulation, the new predictions, as shown in Fig. 11, become more in line with the reconstructed states, even for previously low probability parameters in the pre-flight prediction such as dynamic pressure. It should be noted that the percentiles shown in the figure are compared to the pre-flight prediction not the post-reconciliation predictions.

Another change incorporated within the final reconciled Monte Carlo is a change in the distribution of a parameter that controls the inflation time [27]. For SR01, there was scant data to predict the inflation time of a supersonic parachute in the wake of a slender body. So based on DGB data from previous flights where the payload had been blunt bodies, a rather large dispersion of inflation time was selected for SR01. However, post SR01, the inflation model was adjusted to match flight data and the dispersion was reduced. This updated inflation model was used in Fig. 11(d) and led to a closer match in inflation time in the reconciled simulation than the pre-flight prediction. In the next section, the performance of this updated model setting can be seen when SR02 flight data is analyzed.

The nominal case for the final reconciliation Monte Carlo – with updated atmosphere and separation states – also compares well with the NIACS flight command history recorded on-board. Figure 12 shows the firing command history from the flight and its equivalent from the nominal case of the reconciled Monte Carlo. In the figure, +1 or -1 means a thruster is on, and a 0 means a thruster is off. Although the thruster firings are not identical between the flight data and the simulation, on a macroscopic level the firing histories line up in time. The comparison of the integrated NIACS firing time from the flight data and simulation in Table 4 does not show an exact match; however, the differences are not unreasonable considering one is comparing a single Monte Carlo case to the flight data and the integrated times show that the NIACS in flight behaved similarly to the NIACS modeled in the simulation over the course of the 60 s long coast phase. V0 and V180 are the pitch thrusters, V90 and V270 are the yaw thrusters, VCW and VCCW are the roll

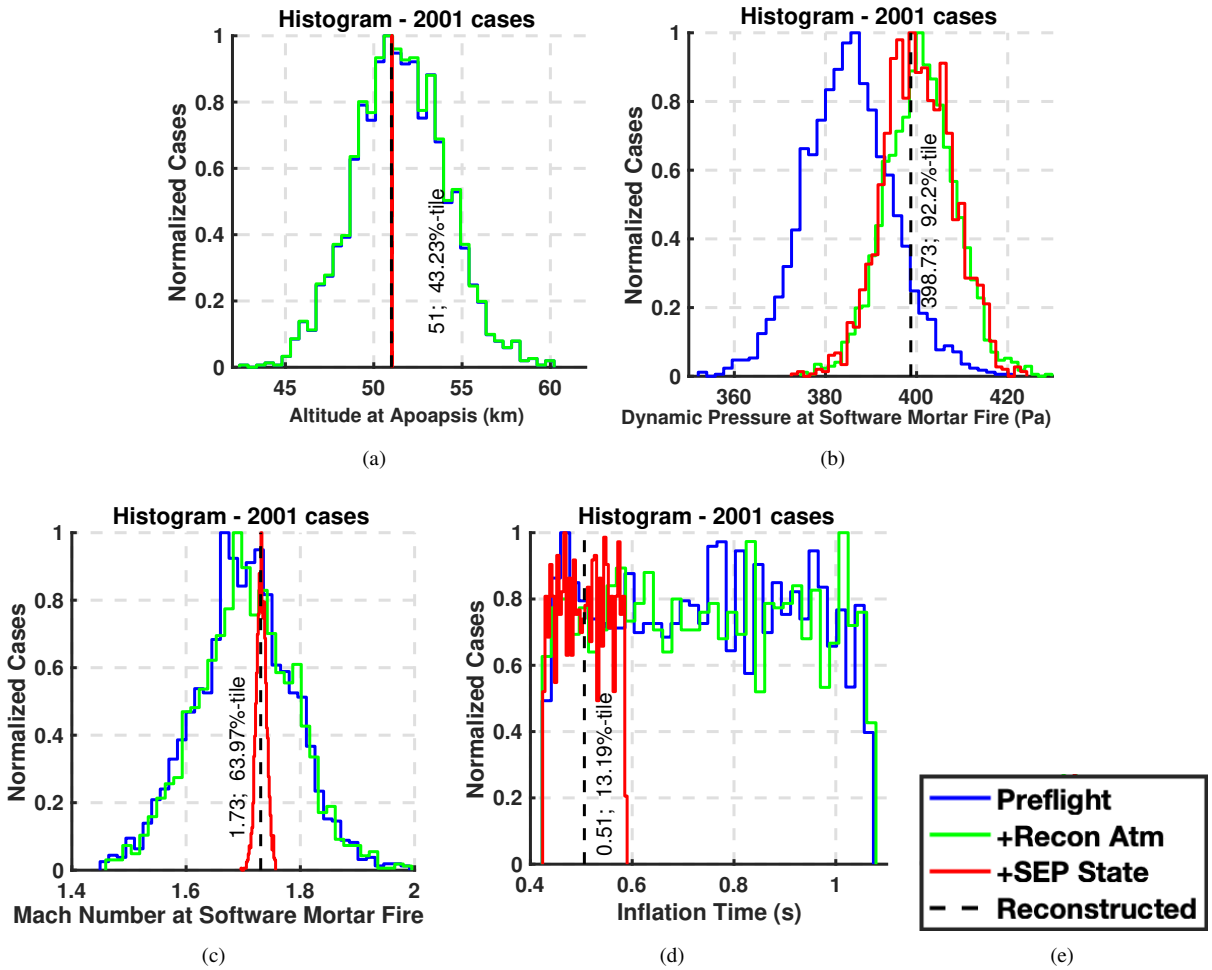

Fig. 11 Reconciliation results for ASPIRE SR01. Reconstruction (black dashed line) shows the percentile compared to the pre-flight prediction.

thrusters that rotate the vehicle in clockwise or counter-clockwise directions, while the VSuper command is a multiplier on all pitch and yaw thrusters when larger controllability is needed.

The ground traces are compared in Fig. 13, where the pre-flight prediction used for recovery and the reconciliation Monte Carlo nominal are co-plotted with the BET profile. Both the pre-flight and reconciliation simulation trajectories are within 0.5 nautical miles of the GPS splashdown location, demonstrating the nominal nature of the SR01 flight. For reference, the 99th percentile confidence splashdown ellipse was 14 by 12 nautical miles in major and minor axis.

Some of the trajectory states from the reconciliation Monte Carlo nominal are co-plotted with the BET profile in Fig. 14. The focus here is during the experiment part of the flight, which includes the coast phase and the parachute deployment phase (100 s to 200 s after launch). Once atmosphere and separation states are adjusted in the simulation, the reconciliation simulation is comparable to the BET states.

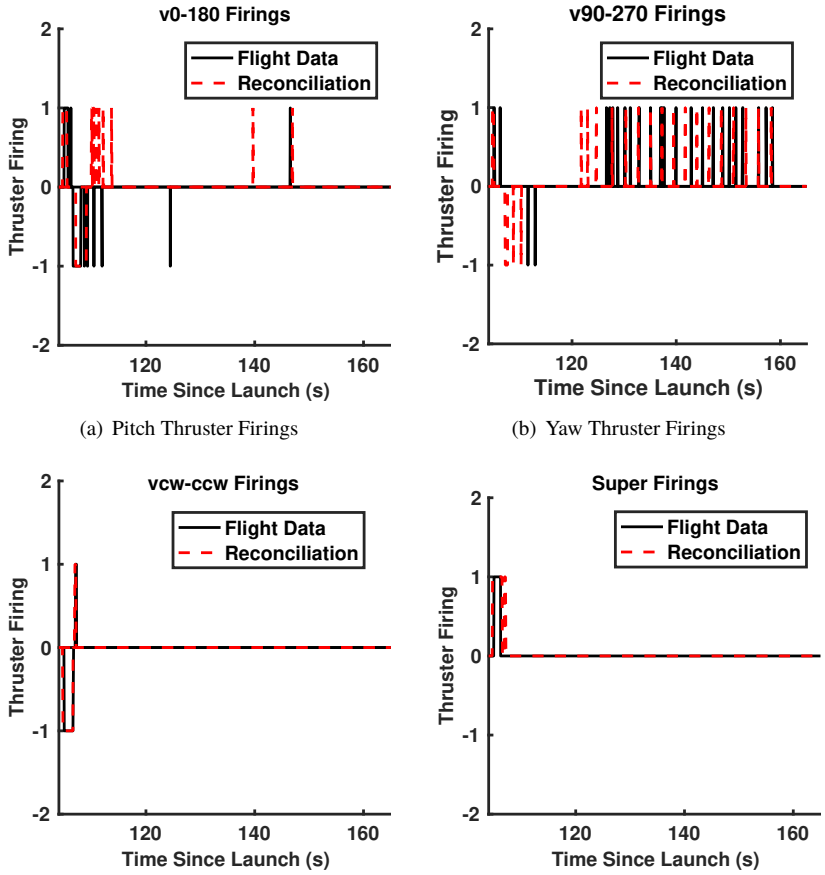

(a) Pitch Thruster Firings

(b) Yaw Thruster Firings

(c) Roll Thruster Firings

(d) Super Thruster Firings

Fig. 12 NIACS firing history reconciliation results for ASPIRE SR01.

Table 4 NIACS integrated firing timing for ASPIRE SR01.

Thruster Name	Flight Data (s)	Reconciliation (s)
v0	0.760	1.390
v90	1.000	1.020
v180	1.620	1.970
v270	0.100	0.540
vcw	0.180	0.210
vccw	1.720	1.850
vsuper	1.220	0.800

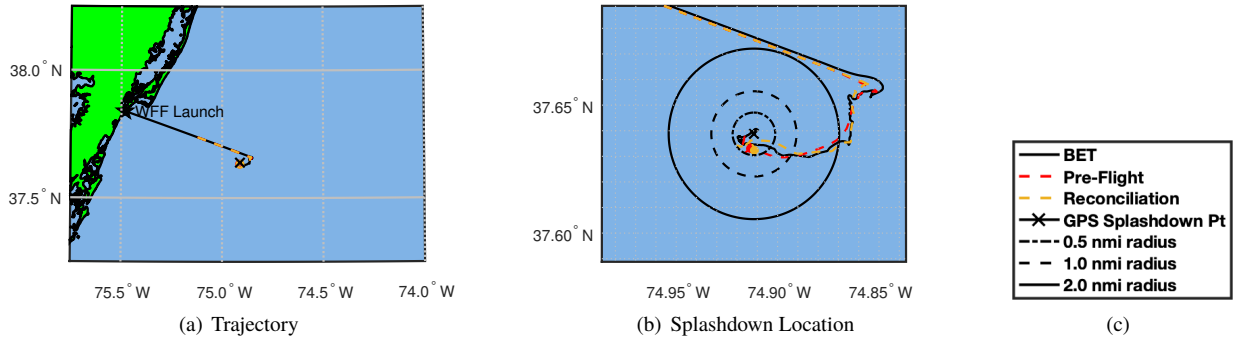

(a) Trajectory (b) Splashdown Location (c)

Fig. 13 Ground trace comparison between BET and simulation for ASPIRE SR01.

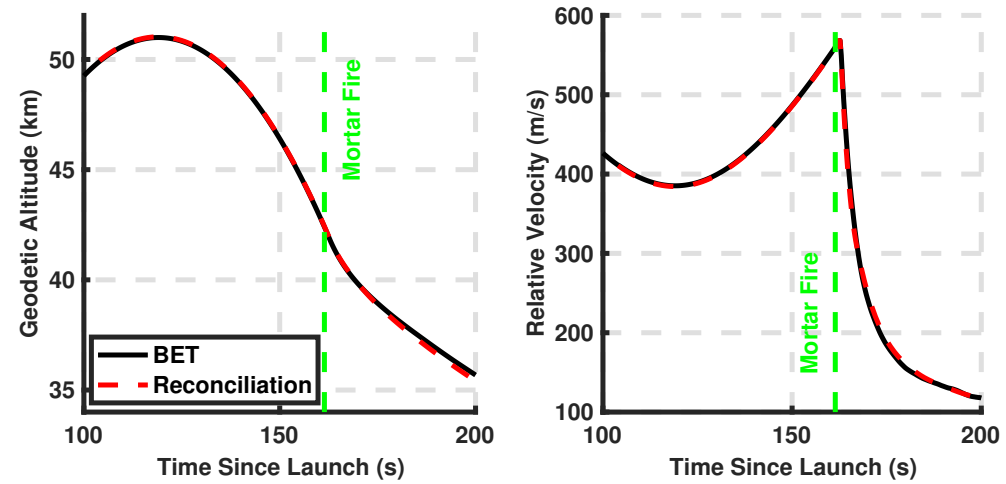

(a) Geodetic Altitude (b) Planet Relative Velocity

(c) Planet Relative Flight Path Angle (d) Pitch Angle

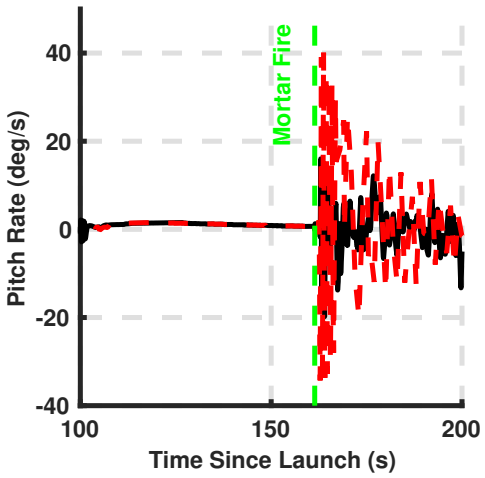

(e) Yaw Rate

Fig. 14 Trajectory comparison between BET and simulation for ASPIRE SR01.

B. ASPIRE SR02 Reconstruction and Reconciliation

The reconstructed trajectory of the ASPIRE SR02 prior to payload separation is summarized in Table 5 and Table 6 shows reconstructed and its pre-flight predictions for events post ASPIRE separation from the sounding rocket. For reference, recall that the targets on-board the flight vehicle were generated one day prior to the day-of-launch (L-1) for 8:00 AM local time launch, although the flight actually flew closer to noon. So, the pre-flight Monte Carlo prediction presented here is for an 8:00 AM launch time. The boosters in ASPIRE SR02 over-performed and led to a higher separation altitude and velocity than the nominal prediction, leading to a trajectory that lofted more than expected. The apogee altitude was 96th percentile of the pre-flight expected distribution. Looking at the trajectory states at events through mortar fire, the flight mechanics simulation pre-flight predictions underestimate the reconstructed BET conditions like Mach number, dynamic pressure, and altitude.

Table 5 ASPIRE SR02 trajectory conditions prior to payload separation

Event	**Time from Launch** *sec*	**Mach**	**Dynamic Pressure** *Pa*	**Wind-Relative Velocity** *m/s*	**Geodetic Altitude** *km*	**Flight Path Angle** *deg*
Launch	0.000	0.02	33.27	7.19	-0.03	5.7
Spin Up	1.188	0.21	3298.22	71.68	0.01	75.6
Terrier Burnout	6.205	0.84	44221.51	278.29	1.06	72.0
Brant Ignition	7.958	0.78	36103.35	256.95	1.50	71.6
Mach 1.0	11.698	1.00	52522.03	330.64	2.54	71.5
Mach 2.0	22.845	2.00	109113.38	617.98	7.45	71.2
Mach 3.0	30.307	3.00	110459.42	888.61	12.70	68.9
Brant Burnout	34.097	3.38	82924.79	994.66	16.07	67.3
Despin Begin	100.027	1.29	65.22	415.95	52.18	32.7

Table 6 ASPIRE SR02 pre-flight prediction and reconstruction of post ASPIRE separation

Item	Units	Pre-Flight Prediction			Flight	Percentile
		1%-tile	50%-tile	99%-tile		
Payload separation						
Mach		0.89	1.09	1.28	1.24	96.45
Dynamic pressure	Pa	30.98	62.69	137.01	53.80	30.83
Wind-relative velocity	m/s	287.84	352.95	413.63	398.06	95.40
Geodetic altitude	km	44.43	49.30	54.48	53.00	96.35
Flight path angle	deg	11.91	22.18	34.42	28.00	87.96
Apogee						
Time from launch	s	112.19	118.72	125.59	123.49	95.85
Mach		0.76	1.00	1.21	1.10	86.06
Dynamic pressure	Pa	15.18	46.74	118.45	33.62	22.59
Wind-relative velocity	m/s	245.16	323.36	389.55	353.25	84.06
Geodetic altitude	km	44.75	50.34	56.72	54.82	96.15
NIACS trigger						
Time from launch	s	147.99	164.89	181.16	176.01	94.70
Mach		1.52	1.72	1.92	1.92	99.00
Dynamic pressure	Pa	503.71	530.93	557.54	567.13	99.90
Wind-relative velocity	m/s	478.72	544.55	614.10	613.20	98.85
Geodetic altitude	km	38.48	40.16	41.83	41.62	98.50
Flight path angle	deg	-61.37	-51.97	-40.95	-55.10	22.54
Mortar fire						
Time from launch	s	149.60	166.50	182.79	177.59	94.65
Mach		1.57	1.76	1.97	1.97	98.95
Dynamic pressure	Pa	580.74	617.49	649.36	670.63	99.95
Wind-relative velocity	m/s	490.29	556.25	627.34	626.75	99.00
Geodetic altitude	km	37.90	39.43	40.94	40.77	98.45
Flight path angle	deg	-62.06	-52.93	-42.20	-55.80	23.89
Line stretch						
Time from launch	s	150.57	167.48	183.77	178.63	94.80
Mach		1.61	1.80	2.01	2.00	98.75
Dynamic pressure	Pa	643.26	687.48	727.99	744.57	99.85
Wind-relative velocity	m/s	501.57	567.30	637.98	636.42	98.80
Geodetic altitude	km	37.51	38.97	40.40	40.27	98.50
Flight path angle	deg	-62.47	-53.50	-42.96	-56.20	24.99
Full inflation						
Time from launch	s	151.03	167.99	184.27	179.08	94.55
Mach		1.56	1.76	1.98	1.97	98.80
Dynamic pressure	Pa	625.79	676.73	725.01	746.50	99.95
Wind-relative velocity	m/s	486.55	552.77	626.44	626.07	98.95
Geodetic altitude	km	37.31	38.74	40.14	40.03	98.75
Flight path angle	deg	-62.66	-53.65	-43.26	-56.40	24.64
Parachute load	lbf	40,043	46,966	54,493	50,491	80.06
Mach 1.4						
Time from launch	s	151.48	168.94	186.13	180.72	95.00
Dynamic pressure	Pa	396.15	453.74	532.13	416.55	7.65
Wind-relative velocity	m/s	434.12	439.07	444.13	444.26	99.10

Item	Units	Pre-Flight Prediction			Flight	Percentile
		1%-tile	50%-tile	99%-tile		
Geodetic altitude	km	37.18	38.32	39.28	39.31	99.15
Flight path angle	deg	-62.85	-53.61	-43.54	-56.90	20.44
Mach 1.0						
Time from launch	s	153.08	170.89	188.48	182.87	95.00
Dynamic pressure	Pa	222.03	251.45	290.32	233.10	7.75
Wind-relative velocity	m/s	308.72	312.59	315.65	316.05	99.60
Geodetic altitude	km	36.68	37.73	38.60	38.63	99.25
Flight path angle	deg	-63.86	-53.79	-42.74	-59.40	9.65
Nose cone jettison						
Time from launch	s	1330.40	1440.80	1607.06	1568.47	93.75
Mach		0.03	0.03	0.04	0.03	7.15
Splashdown*						
Time from launch	s	1750.25	1914.87	2123.57	2029.57	83.56
Mach		0.02	0.02	0.02	0.02	83.71
Flight path angle	deg	-50.54	-30.76	-20.60	-49.30	1.65

Comparing predictions with the BET at line stretch and full inflation events show that the pre-flight prediction under-predicted atmospheric-based conditions like Mach number and dynamic pressure, although other reconstructed states like the splashdown time seem to be within the bounds of the pre-flight predictions. The SR02 flight had a higher than expected separation altitude and the atmosphere used in the flight software was for 8:00 AM instead of the launch time of 12:00 PM. It was expected that adjusting for separation states and atmosphere in the reconciliation Monte Carlo would affect its comparison with the reconstructed data. During post-flight analysis, a discrepancy in the altitude definition between the forecast and simulation was also discovered that created a small error in altitude. This discrepancy was present for SR01, but was not observed until reconciliation for SR02. The results in Sec. VI.A have not been adjusted for the error to preserve observations made after SR01 reconstruction in preparation for SR02. In general, the discrepancy was not large enough to change any observations or trends made after SR01, but for thoroughness the change was made in preparation for SR03. Through the altitude convention change and the time of day effect on atmospheric parameters, the large difference seen in atmospheric-based states were resolved between the reconstructed values and the reconciled states, as seen in Fig. 15. Recall that the inflation time model was adjusted after SR01 based on data from that flight. That model seems to perform well in SR02 (Fig. 15(d)).

A small subset of the trajectory states from the reconciliation Monte Carlo nominal are co-plotted with the BET profile in Fig. 16. Once again, the focus here is during the experiment part of the flight, which includes the coast phase and the parachute deployment phase (100 s to 200 s after launch). Although SR02 was not as close to the nominal pre-flight prediction as SR01 due to differences in the atmosphere and separation states, one can see that once

*Loss of signal for SR02 was at 1967 s from launch and 385 m altitude. Splashdown conditions were computed by propagating the states down to 0 km altitude to make comparisons with the pre-flight simulation.

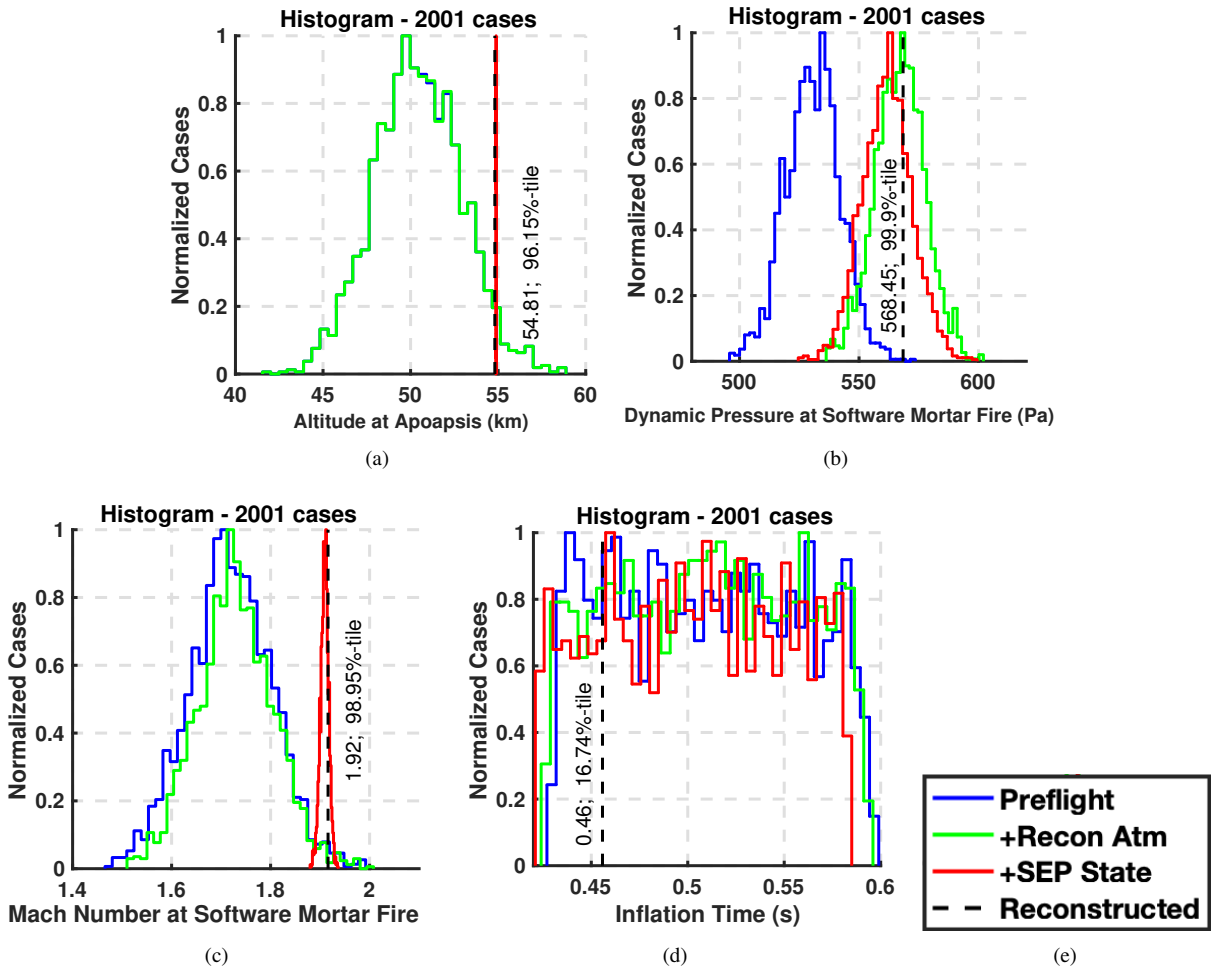

Fig. 15 Reconciliation results for ASPIRE SR02. Reconstruction (black dashed line) shows the percentile compared to the pre-flight 8:00 AM prediction.

atmosphere and separation states are adjusted in the simulation to match the day-of-launch data, the reconciliation simulation is comparable to the BET states.

The ground traces for the SR02 BET, pre-flight predictions, and reconciliation Monte Carlo nominal tracks are compared in Fig. 17. Unlike SR01, the comparison between BET and the simulation profiles are not as close due to differences in atmosphere. Due to dynamic wind conditions at low altitudes not captured in the forecast, the simulation did not predict the splashdown point with the same accuracy as was seen for SR02.

Based on pre-flight meteorological analyses, significant changes in the atmospheric states were not expected to occur at the time scale of several hours at the altitudes of interest (30-45km). However, for SR02, the vehicle was launched between two significant weather systems moving through the WFF area, leading to an atypically dynamic atmosphere. Thus, the actual weather at noon was outside the requirement window of the 8:00 AM weather for which the dynamic pressure targets were generated. In retrospect, the targeted states should have been updated when the launch

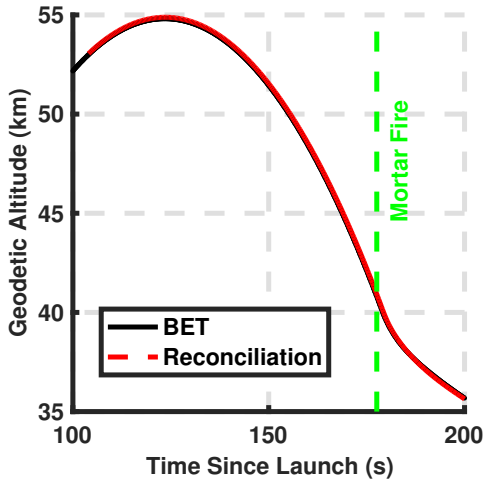

(a) Geodetic Altitude

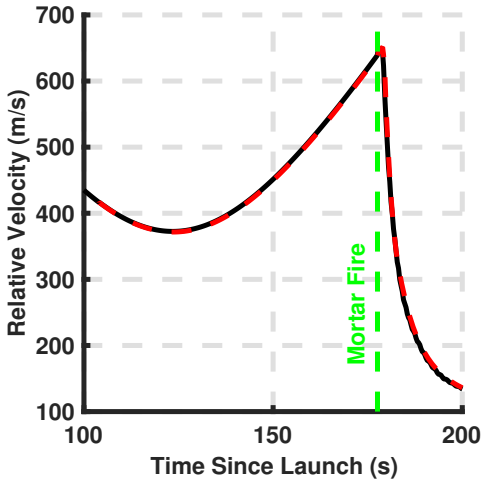

(b) Planet Relative Velocity

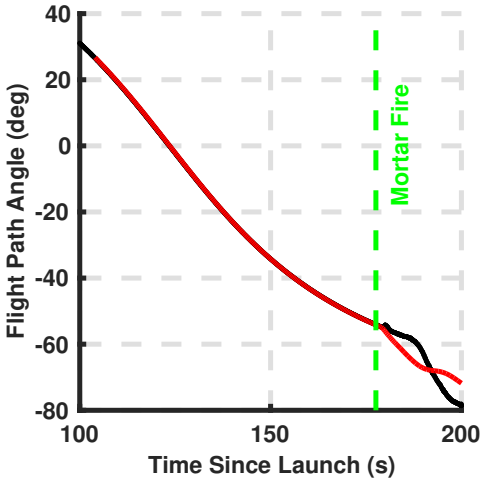

(c) Planet Relative Flight Path Angle

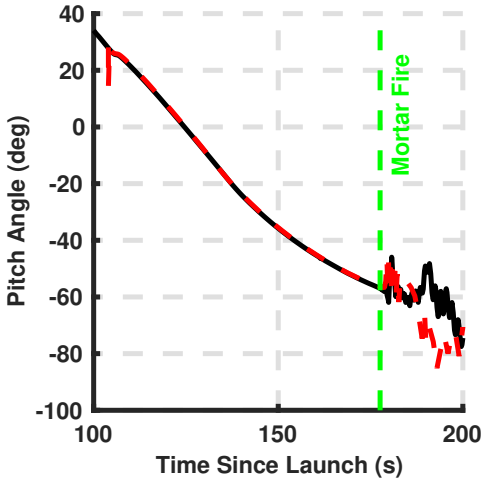

(d) Pitch Angle

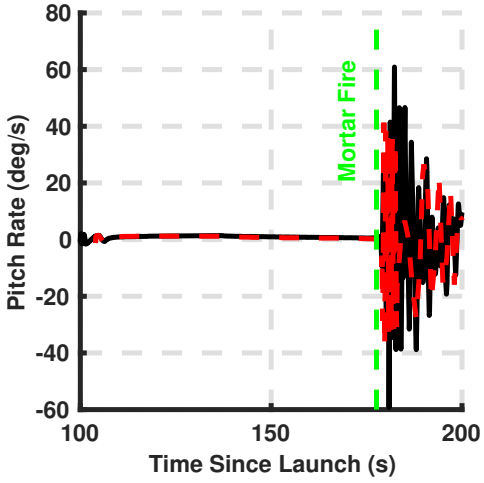

(e) Yaw Rate

Fig. 16 Trajectory comparison between BET and simulation for ASPIRE SR02.

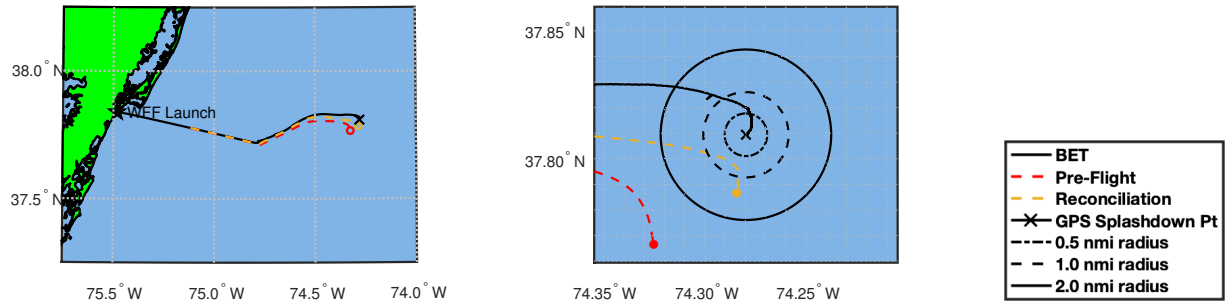

(a) Trajectory (b) Splashdown Location (c)

Fig. 17 Ground trace comparison between BET and simulation for ASPIRE SR02.

time window changed from L-1 day targeting.

C. ASPIRE SR03 Reconstruction and Reconciliation

The reconstructed trajectory of the ASPIRE SR03 is summarized in Tables 7 and 8. The targets on-board the flight vehicle were generated on L-1 day for an 11:00 AM launch and the actual flight was flown around 9:30 am. The pre-flight Monte Carlo prediction presented here is for a 11:00 AM launch time.

Table 7 ASPIRE SR03 trajectory conditions at key test events

Event	Time from Launch	Mach	Dynamic Pressure	Wind-Relative Velocity	Geodetic Altitude	Flight Path Angle
	sec		*Pa*	*m/s*	*km*	*deg*
Launch	0.000	0.03	59.42	10.00	-0.041	-4.97
Spin Up	1.112	0.18	2317.96	62.54	-0.007	69.66
Terrier Burnout	5.547	0.82	44160.69	283.71	0.845	74.56
Brant Ignition	8.029	0.74	33439.68	254.14	1.483	73.49
Mach 1.0	12.217	1.00	52656.25	339.32	2.666	71.97
Mach 2.0	23.647	2.00	109494.76	639.81	7.840	68.50
Mach 3.0	30.697	3.00	120011.05	883.27	12.764	66.56
Brant Burnout	33.725	3.29	94687.38	946.14	15.334	66.15
Despin Begin	100.150	1.21	111.61	387.02	47.560	23.95

Table 8 ASPIRE SR03 pre-flight prediction and reconstruction of post ASPIRE separation

Item	Units	Pre-Flight Prediction			Flight	Percentile
		1%-tile	50%-tile	99%-tile		
Payload separation						
Mach		0.92	1.14	1.34	1.17	63.47
Dynamic pressure	Pa	55.49	114.50	255.27	96.41	30.68
Wind-relative velocity	m/s	293.68	365.24	427.84	372.53	60.12
Geodetic altitude	km	41.58	46.38	50.63	48.10	81.71
Flight path angle	deg	6.83	17.14	28.51	18.69	63.07

Item	Units	Pre-Flight Prediction			Flight	Percentile
		1%-tile	50%-tile	99%-tile		
Apogee						
Time from launch	s	108.64	114.99	120.55	116.53	72.36
Mach		0.86	1.09	1.29	1.11	59.47
Dynamic pressure	Pa	36.95	97.35	248.46	79.36	30.98
Wind-relative velocity	m/s	275.86	349.72	413.55	354.82	58.02
Geodetic altitude	km	41.69	46.96	51.94	48.85	80.61
Mortar fire						
Time from launch	s	142.00	159.29	173.39	163.82	75.06
Mach		1.58	1.76	1.93	1.85	88.81
Dynamic pressure	Pa	852.10	900.92	948.68	931.71	91.95
Wind-relative velocity	m/s	491.04	547.98	603.74	575.79	87.16
Geodetic altitude	km	36.12	37.51	38.76	38.12	86.81
Flight path angle	deg	-60.88	-51.25	-39.79	-51.86	44.23
Line stretch						
Time from launch	s	142.99	160.27	174.38	164.85	75.31
Mach		1.61	1.79	1.97	1.88	87.71
Dynamic pressure	Pa	931.01	995.15	1056.61	1028.44	89.81
Wind-relative velocity	m/s	501.38	558.84	614.34	584.67	85.76
Geodetic altitude	km	35.76	37.09	38.28	37.65	85.71
Flight path angle	deg	-61.35	-51.84	-40.65	-52.54	43.83
Full inflation						
Time from launch	s	143.54	160.79	174.94	165.26	74.36
Mach		1.54	1.72	1.91	1.85	94.50
Dynamic pressure	Pa	872.50	949.46	1024.35	1020.12	98.60
Wind-relative velocity	m/s	478.93	536.60	596.27	573.21	92.30
Geodetic altitude	km	35.55	36.87	38.00	37.45	87.76
Flight path angle	deg	-61.59	-52.24	-41.31	-52.77	44.78
Parachute load	lbf	55,724	66,059	77,084	67,369	57.47
Mach 1.4						
Time from launch	s	143.84	161.44	175.87	166.15	75.36
Dynamic pressure	Pa	567.97	648.85	764.27	615.49	19.39
Wind-relative velocity	m/s	431.98	436.21	440.08	434.46	15.24
Geodetic altitude	km	35.47	36.62	37.57	37.10	86.66
Flight path angle	deg	-62.59	-52.82	-41.38	-53.94	40.63
Mach 1.0						
Time from launch	s	145.17	162.91	177.47	167.59	75.06
Dynamic pressure	Pa	308.90	350.35	408.07	333.60	20.04
Wind-relative velocity	m/s	308.13	311.25	314.27	311.55	58.97
Geodetic altitude	km	35.16	36.22	37.13	36.67	86.86
Flight path angle	deg	-64.91	-54.30	-42.61	-55.78	38.58
Nose cone jettison						
Time from launch	s	1302.01	1406.34	1564.50	1485.82	82.36
Mach		0.03	0.03	0.04	0.03	2.30
Flight path angle	deg	-88.08	-74.39	-54.02	-78.91	30.13
Splashdown						
Time from launch	s	1710.36	1865.83	2066.48	1982.22	84.41
Mach		0.02	0.02	0.02	0.02	78.86

Item	Units	Pre-Flight Prediction			Flight	Percentile
		1%-tile	50%-tile	99%-tile		
Flight path angle	deg	-85.94	-62.17	-33.72	-69.78	27.94

For SR01 and SR02, the boosters over performed during the powered stage, leading to higher energy states at ASPIRE separation than the pre-flight expectation. Prior to SR03, the performance of the ASPIRE flights and few other recent sounding rocket tests with the same configuration were used to adjust the expected powered flight states. One can see that the adjustments brought Mach and wind-relative velocity at payload separation closer to the median for SR03 compared to their equivalent performance for SR01 and SR02. However, looking at the trajectory states at events through mortar fire, the flight mechanics simulation pre-flight predictions still underestimate the reconstructed BET conditions like Mach number, dynamic pressure, and altitude. The pre-SR03 flight update to the initial states estimate was based on a dearth of data to try to correct a situation observed in a handful of flights; it is expected that with more booster flights, the prediction model will be improved and the estimates for the powered flight states would be adjusted up to reduce the over prediction.

During reconciliation, the true separation states and reconstructed atmospheric profiles were incorporated with the flight mechanics tool to update the simulation predictions. Figure 18 shows that lower probability pre-flight simulation predictions like dynamic pressure at mortar fire were improved once flight observables were incorporated during reconciliation, similar to what was seen for SR01 and SR02. Specifically, since atmospheric-relative quantities were under predicted in the simulation, using reconstructed atmosphere improved the simulation prediction.

One metric of interest that did not reconcile as well as in previous flights was the parachute inflation time. The model for this variable was modified from SR01 and SR02 and then held constant for SR03. More investigation is needed to understand if there are other factors that affect inflation time and how it is modeled in simulations.

The reconciled Monte Carlo nominal trajectory for SR03 is compared with the BET in Figure 19 during the science phase of the flight. Once atmospheric states and separation states are incorporated in the simulation, the trajectory from the flight mechanics tool looks comparable to the BET.

The ground traces for the SR03 BET, pre-flight predictions, and reconciliation Monte Carlo nominal tracks are compared in Fig. 20. Updating separation states and atmospheric states, especially the wind model, reconciled the simulation with the as-flown trajectory.

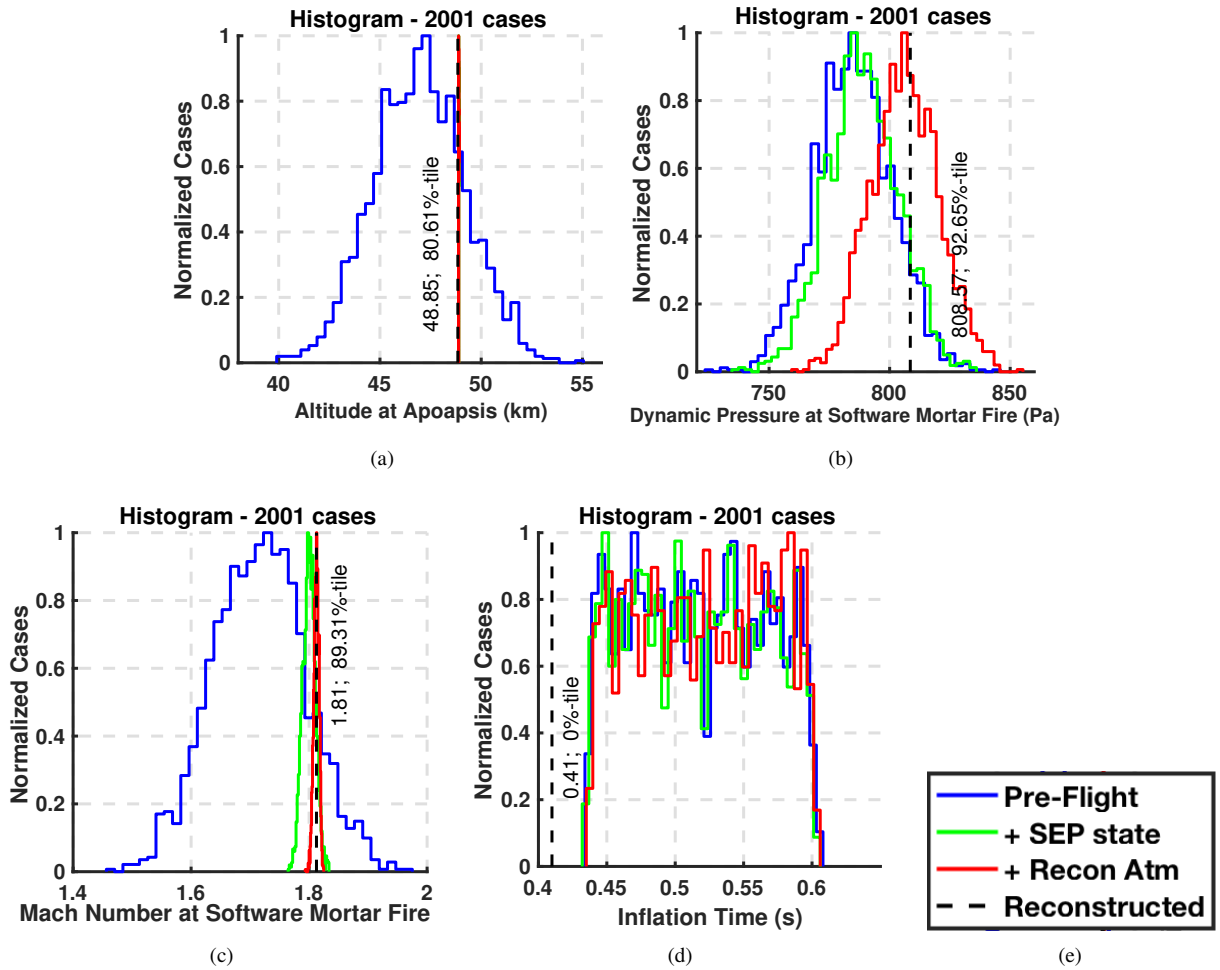

Fig. 18 Reconciliation results for ASPIRE SR03. Reconstruction (black dashed line) shows the percentile compared to the pre-flight 11:00 AM prediction.

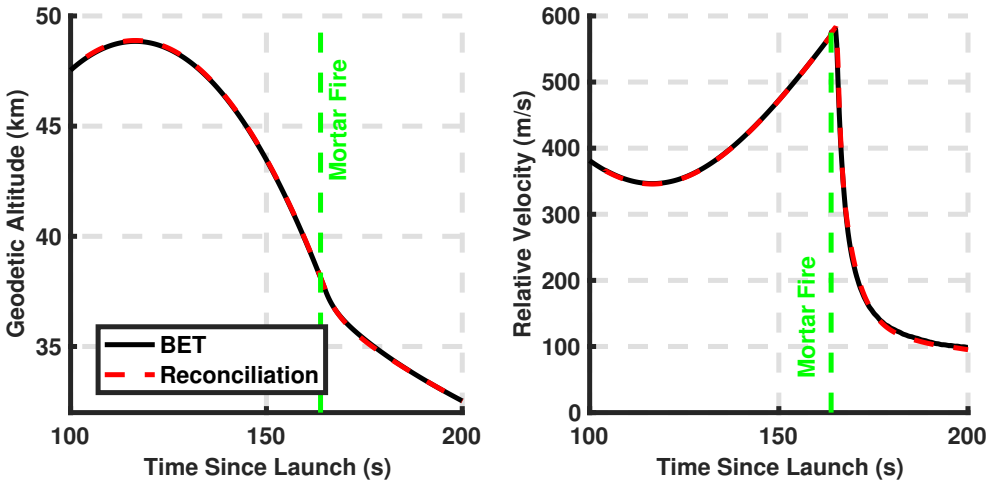

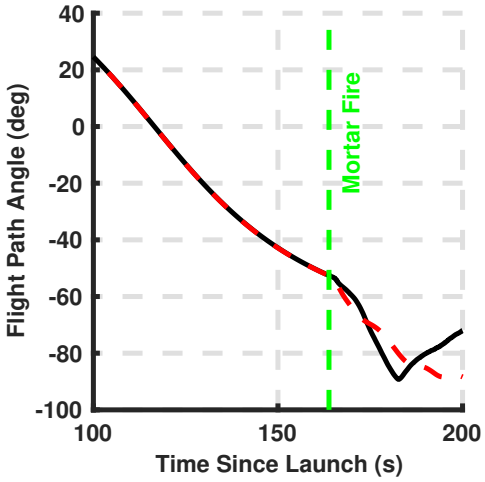

(c) Planet Relative Flight Path Angle

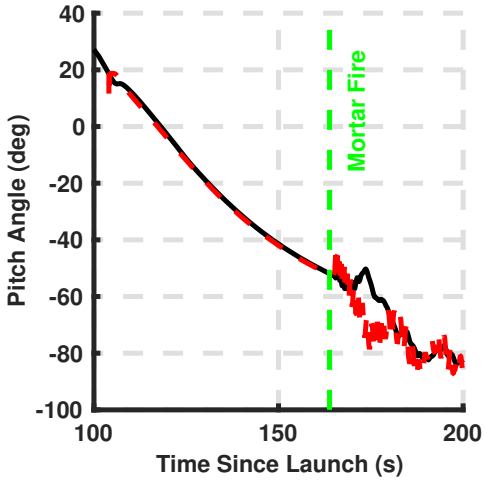

(d) Pitch Angle

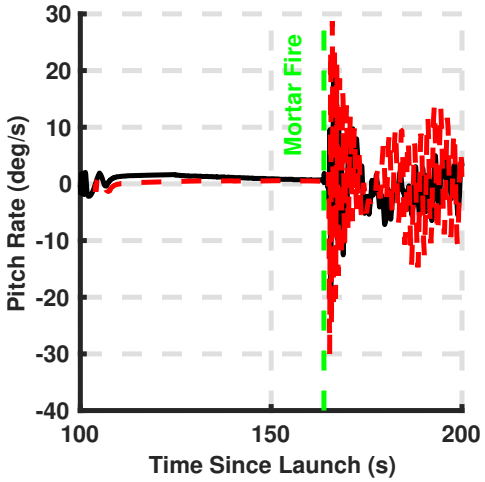

(e) Yaw Rate

Fig. 19 Trajectory comparison between BET and simulation for ASPIRE SR03.

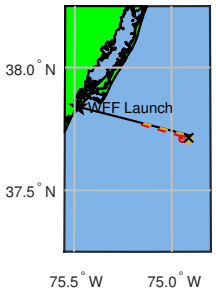

(a) Trajectory

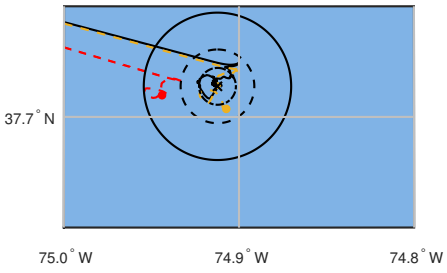

(b) Splashdown Location

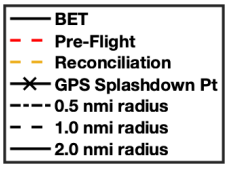

(c)

Fig. 20 Ground trace comparison between BET and simulation for ASPIRE SR03.

D. Model changes for simulation based on reconstruction

Overall, once simulations were adjusted for conditions not known *a priori* - such as the actual atmospheric condition during flight or the actual separation state of the ASPIRE payload from the booster - the updated simulation results matched the reconstructed states. Thus, there were very few model change recommendations for future flights coming from the analysis of the data. There were few reasons to suggest any changes in the aerodynamics of the payload based on the flight data. The NIACS models in the simulation also performed close to the flight data recorded in the ASPIRE flights. The aerosciences team recommended tailoring the uncertainties and shape of the nominal parachute drag force based on the reconstructed trajectory [23]. However, there were not recommended changes for the static parachute aerodynamic tables which largely define the parachute force history in 6-DOF simulations. In general, many model changes are not recommended for future applications of these simulations in similar sounding rocket tests.

E. Lessons Learned

Although there were not many model change recommendations from the ASPIRE flight, there were some lessons learned. The vehicle performance was very sensitive to initial conditions, and the booster performance was overpredicted in all three flights. Updating the booster performance to decrease the overprediction would be important for future flights.

The SR02 flight also showed the importance of understanding the sensitivity of targets due to atmospheric states. For SR03, the team prepared for changing atmospheric conditions by creating targets for multiple launch times. However, these targets were created in increments of 3 hours, since the atmospheric predictions are generated in those temporal resolution. If flight performance are found to be sensitive to small changes in atmospheric states in between the 3 hour increments when atmospheric predictions are available, custom atmospheric products might be required.

There were also challenges in reconstruction for certain areas, such as the payload aerodynamics [23]. The payload produces a very small force history, which was distinguish from noise in the presence of large uncertainties in atmospheric states. Direct measurement of the pressure distribution on the payload using sensors like flush air data systems could improve aerodynamic reconstruction and separate atmospheric and aerodynamic uncertainties currently enmeshed together in the reconstructed states.

VII. Conclusions

The ASPIRE project was a series of sounding rocket tests that were designed as a risk reduction exercise for the supersonic parachute for Mars 2020. In October 2017, ASPIRE SR01 tested the MSL build-to-print print DGB parachute and deployed the decelerator near conditions seen by the MSL mission on Mars in 2012. In March and September 2018, ASPIRE SR02 and SR03 successfully demonstrated the strengthened DGB parachute for Mars 2020 at a dynamic pressure that was 50% and 100% higher than what was seen for MSL. A multi-body flight dynamics

simulation was developed to provide pre-flight vehicle performance predictions and was used to target Mars relevant parachute deployment conditions for all three flights. The simulation incorporated various engineering models, such as 6-DOF test vehicle aerodynamics, 6-DOF parachute aerodynamics, NIACS attitude control system models, and atmospheric prediction models. For all three flights, the simulation provided data to accurately target desired metrics, and the data products assisted range safety and recovery operations.

Post-flight reconstruction was completed after each flight to provide data used to validate the pre-flight dynamics simulation and improve the design of future flights. There were few modeling changes that were needed to improve predictions from the simulation between flights. It was found that after adjusting the simulations for flight observables not known before the flight, such as booster performance and atmospheric conditions, the simulation predictions compared well with the best estimated trajectory. Based on the observed flight performances from the three ASPIRE flights, no modeling changes are recommended to improve predictions for future flights planned for follow-on missions from the ASPIRE program and the Mars 2020 flight.

Acknowledgments

Several ASPIRE team members have contributed to the flight mechanics and reconstruction work presented in this paper. These team members include Ian Clark, Christopher Tanner, John Van Norman, Suman Muppidi, Juan Cruz, William Strauss, Nicholas Marks, William Colson, and David Way. Parts of this research were carried out at the Jet Propulsion Laboratory, California Institute of Technology, under a contract with NASA.

References

[1] Cruz, J. R., Way, D. W., Shidner, J. D., Davis, J., Adams, D. S., and Kipp, D., "Reconstruction of the Mars Science Laboratory Parachute Performance," *Journal of Spacecraft and Rockets*, Vol. 51, No. 4, 2014, pp. 1185–1196.

[2] Karlgaard, C. D., Kutty, P., O'Farrell, C., Blood, E., Ginn, J., , and Schoenenberger, M., "Reconstruction of Atmosphere, Trajectory, and Aerodynamics for the Low-Density Supersonic Decelerator Project," *Journal of Spacecraft and Rockets*, Vol. 56, No. 1, 2019, pp. 221–240.

[3] Tanner, C., Clark, I., , and Chen, A., "Overview of the Mars 2020 Parachute Risk Reduction Plan," *IEEE Aerospace Conference 2018,* Big Sky, MT, 2018.

[4] "NASA Sounding Rocket Program Handbook," Tech. Rep. 810-HB-SRP, Sounding Rockets Program Office, Suborbital and Special Orbital Projects Directorate, Goddard Space Flight Center, Wallops Flight Facility, Wallops Island, Virginia, 2005.

[5] Karlgaard, C., Tynis, J., and O'Farrell, C., "Reconstruction of the Advanced Supersonic Parachute Inflation Research Experiment (ASPIRE) Sounding Rocket Flight Test," AIAA Paper No. 2018-3624 *AIAA Atmospheric Flight Mechanics Conference,* Atlanta, GA, 2018.

[6] Karlgaard, C. D., Tynis, J., O'Farrell, C., and Sonneveldt, B., "Reconstruction of the Advanced Supersonic Parachute Inflation Research Experiment Sounding Rocket Flight Test with Strengthened Disk-Gap-Band Parachute," AIAA 2019-0014*, AIAA SciTech 2019, AIAA Atmospheric Flight Mechanics Conference,* San Diego, CA, 2019.

[7] Sonneveldt, B., O'Farrell, C., and Clark, I., "Summary of the Advanced Supersonic Parachute Inflation Research Experiments (ASPIRE) Sounding Rocket Tests with a Disk-Gap-Band Parachute," AIAA 2019-3482*, AIAA SciTech 2019, AIAA Atmospheric Flight Mechanics Conference,* San Diego, CA, 2019.

[8] Ivanov, M., and Tibbets, B., "Low Density Supersonic Decelerator Flight Dynamics Test - 1 Flight Design and Targeting," AIAA 2015-2152*, AIAA Aerodynamic Decelerator Systems Conference,* Daytona Beach, FL, 2015.

[9] Strauss, W., "Construction of Supersonic Flight Dynamics Test Vehicle Monte Carlo Splashdown Footprints for use in Range Safety and Recovery Operations," AAS 16-288*, AAS/AIAA Space Flight Mechanics Conference,* Napa, CA, 2016.

[10] Braun, R. D., Powell, R. W., Engelund, W. C., Gnoffo, P. A., Weilmuenster, K. J., and Mitcheltree, R. A., "Mars Pathfinder Six-Degree-of-Freedom Entry Analysis," *Journal of Spacecraft and Rockets*, Vol. 32, No. 6, 1995, pp. 993–1000. doi: 10.2514/3.26720.

[11] Desai, P. N., Schoenenberger, M., and Cheatwood, F. M., "Mars Exploration Rover Six-Degree-of-Freedom Entry Trajectory Analysis," *Journal of Spacecraft and Rockets*, Vol. 43, No. 5, 2006, pp. 1019–1025. doi:10.2514/1.6008.

[12] Desai, P. N., Prince, J. L., Queen, E. M., Schoenenberger, M., Cruz, J. R., and Grover, M. R., "Entry, Descent, and Landing Performance of the Mars Phoenix Lander," *Journal of Spacecraft and Rockets*, Vol. 48, No. 5, 2011, pp. 798–808. doi:10.2514/1.48239.

[13] Way, D. W., Davis, D., Jody, and Shidner, J. D., "Assessment of the Mars Science Laboratory Entry, Descent, and Landing Simulation," AAS 13-420*, AAS/AIAA Space Flight Mechanics Conference,* Kauai, HI, 2013.

[14] Bowes, A., Davis, J. D., Dutta, S., Striepe, S., Ivanov, M., Powell, R., and White, J. P., "LDSD POST2 Simulation and SFDT-1 Pre-flight Launch Operations Analyses," AAS 15-232, *AAS/AIAA Space Flight Mechanics Conference,* Williamburg, VA, 2015.

[15] White, J., Dutta, S., and Striepe, S., "SFDT-1 Camera Pointing and Sun-Exposure POST2 Analysis and Flight Performance," AAS 15-218, *AAS/AIAA Space Flight Mechanics Conference,* Williamburg, VA, 2015.

[16] Dutta, S., Bowes, A., Striepe, S., Davis, J. D., Blood, E. M., and Ivanov, M., "Supersonic Flight Dynamics Test 1 - Post-flight Assessment of Simulation Performance," AAS 15-219, *AAS/AIAA Space Flight Mechanics Conference,* Williamsburg, VA, 2015.

[17] White, J. P., Bowes, A., Dutta, S., Ivanov, M., and Queen, E., "LDSD POST2 Modeling Enhancements in Support of SFDT-2 Flight Operations," AAS 16-221, *AAS/AIAA Space Flight Mechanics Conference,* Napa, CA, 2016.

[18] Dutta, S., Bowes, A., White, J., Striepe, S., Queen, E., O'Farrell, C., and Ivanov, M., "Post-Flight Assessment of Low Density Supersonic Decelator Flight Dynamics Test 2 Simulation," AAS 16-222, *AAS/AIAA Space Flight Mechanics Conference,* Napa, CA, 2016.

[19] Leslie, F., and Justus, C., "The NASA Marshall Space Flight Center Earth Global Reference Atmosphere Model - 2010 Version," Tech. rep., NASA/TM-2011-216467, 2011.

[20] Molod, A., Takacs, L., Suarez, M., Bacmeister, J., Song, I., and Eichmann, A., "The GEOS-5 Atmospheric General Circulation Model: Mean Climate and Development from MERRA to Fortuna," Tech. Rep. NASA TM 2012-104606-VOL-28, NASA GFSC, 2012.

[21] Toniolo, M., Tartabini, P., Pamadi, B., and Hotchko, N., "Constraint Force Equation Methodology for Modeling Multi-Body Stage Separation Dynamics," AIAA 2008-219, *AIAA Aerospace Sciences Meeting and Exhibit,* Reno, NV, 2008.

[22] Muppidi, S., O'Farrell, C., Tanner, C., Van Norman, J., and Clark, I., "Modeling and Flight Performance of Supersonic Disk-Gap-Band Parachutes In Slender Body Wakes," AIAA Paper No. 2018-3623 *AIAA Aviation Conference 2018,* Atlanta, GA, 2018.

[23] Muppidi, S., O'Farrell, C., Van Norman, J., and Clark, I., "ASPIRE Aerodynamic Models and Flight Performance," AIAA Paper No. 2019-3376 *AIAA Aviation Conference 2019,* Dallas, TX, 2019.

[24] O'Farrell, C., Karlgaard, C., Tynis, J., and Clark, I., "Overview and Reconstruction of the ASPIRE Project's SR01 Supersonic Parachute Test," *IEEE Aerospace Conference,* Big Sky, MT, 2018.

[25] O'Farrell, C., Sonneveldt, B. S., Karlgaard, C., Tynis, J. A., and Clark, I. G., "Overview of the ASPIRE Project's Supersonic Flight Tests of a Strengthened DGB Parachute," *IEEE Aerospace Conference,* Big Sky, MT, 2019.

[26] Cruz, J., Way, D., Shidner, J., Davis, J., Powell, R., Kipp, D., Adams, D., Sengupta, A., Witkowski, A., and Kandis, M., "Parachute Models Used in the Mars Science Laboratory Entry, Descent, and Landing Simulation," AIAA 2013-1276, *AIAA Aerodynamic Decelerator Systems Conference,* Daytona Beach, FL, 2013.

[27] Greene, G., "Opening Distance of a Parachute," *Journal of Spacecraft*, Vol. 7, No. 1, 1970, pp. 98–100. doi:10.2514/3.29878.

[28] Way, D., "A Momentum-Based Indicator for Predicting the Peak Opening Load of Supersonic Parachutes," IEEE Paper No. *IEEE Aerospace Conference,* Big Sky, MT, 2018.

[29] "LMS6 Radiosonde Operator's Manual," Tech. rep., Lockheed Martin Sippican, 2013.

[30] "Guide to Meteorological Instruments and Methods of Observation," Tech. rep., World Meteorological Organization, 2014.

[31] Rienecker, M. M., Suarez, M. J., Todling, R., Bacmeister, J., Takacs, L., Liu, H.-C., Gu, W., Sienkiewicz, M., Koster, R., Gelaro, R., Stajner, I., , and Nielsen, J., "Guide to Meteorological Instruments and Methods of Observation," , 2008.

[32] Bosilovich, M., Lucchesi, R., and Suarezn, M., "MERRA-2: File Specification," , 2016.

[33] Karlgaard, C., Blanchard, R., Kirsch, M., Tartabini, P., and Toniolo, M., "Hyper-X Post-Flight Trajectory Reconstruction," *Journal of Spacecraft and Rockets*, Vol. 43, No. 1, 2006, pp. 105–115. doi:10.2514/1.12733.

[34] Karlgaard, C., Beck, R., Derry, S., Brandon, J., Starr, B., Tartabini, P., and Olds, A., "Ares I-X Trajectory Reconstruction: Methodology and Results," *Journal of Spacecraft and Rockets*, Vol. 50, No. 3, 2013, pp. 641–661. doi:10.2514/1.A32345.

[35] Wagner, W. E., "Re-Entry Filtering, Prediction, and Smoothing," *Journal of Spacecraft and Rockets*, Vol. 3, No. 9, 1966, pp. 1321–1327.

[36] Wagner, W., and Serold, A., "Formulation on Statistical Trajectory Estimation Programs," Tech. rep., NASA CR 1482, 1970. URL `http://en.scientificcommons.org/42645943`.

[37] Olds, A. D., Beck, R. E., Bose, D. M., White, J. P., Edquist, K. T., Hollis, B. R., Lindell, M. C., Cheatwood, F. M., Gsell, V. T., , and Bowden, E. L., "IRVE-3 Post-Flight Reconstruction," AIAA 2013-1390*, AIAA Aerodynamic Decelerator Systems Conference,* Daytona Beach, FL, 2013.

[38] Heck, M. L., Findlay, J. T., Kelly, G. M., , and Compton, H. R., "Adaptation of a Strapdown Formulation for Processing Inertial Platform Data," *Journal of Guidance, Control, and Dynamics*, Vol. 7, No. 1, 1984, pp. 15–19.

[39] Karlgaard, C. D., Tynis, J., and O'Farrell, C., "Reconstruction of the Advanced Supersonic Parachute Inflation Research Experiment Sounding Rocket Flight Test," AIAA 2018-3624*, AIAA Aviation 2018, AIAA Atmospheric Flight Mechanics Conference,* Atlanta, GA, 2018.

[40] Dutta, S., Queen, E., Bowes, A., Leyleck, E., and Ivanov, M., "ASPIRE Flight Mechanics Modeling and Post Flight Analysis," AIAA 2018-3625*, AIAA Aviation 2018, AIAA Atmospheric Flight Mechanics Conference,* Atlanta, GA, 2018.

[41] Leylek, E., "Overview of the ASPIRE Targeting System and Flight Results," *Paper presented at the AAS Guidance, Navigation and Control Conference,* Breckenridge, CO, 2019.